Firn Clutter Constraints on the Design and Performance of Orbital Radar Ice Sounders

Riley Culberg[®], Student Member, IEEE, and Dustin M. Schroeder[®], Senior Member, IEEE

Abstract—Radar sounding is a powerful tool for constraining subglacial conditions, which influence the mass balance of polar ice sheets and their contributions to global sea-level rise. A satellite-based radar sounder, such as those successfully demonstrated at Mars, would offer unprecedented spatial and temporal coverage of the subsurface. However, airborne sounding studies suggest that poorly constrained radar scattering in polar firm may produce performance-limiting clutter for terrestrial orbital sounders. We develop glaciologically constrained electromagnetic models of radar interactions in firn, test them against in situ data and multifrequency airborne radar observations, and apply the only model we find to be consistent with observation to assess the implications of firn clutter for orbital sounder system design. Our results show that in the very high-frequency (VHF) and ultrahigh-frequency (UHF) bands, radar interactions in the firn are dominated by quasi-specular reflections at the interfaces between layers of different densities and that off-nadir backscatter is likely the result of small-scale roughness in the subsurface density profiles. As a result, high frequency (HF) or low VHF center frequencies offer a significant advantage in near-surface clutter suppression compared to the UHF band. However, the noise power is the dominant constraint in all bands, so the near-surface clutter primarily constrains the extent to which the transmit power, pulselength, or antenna gain can be engineered to improve the signal-to-noise ratio. Our analysis suggests that the deep interior of terrestrial ice sheets is a difficult target for orbital sounding, which may require optimizations in azimuth processing and cross-track clutter suppression which complement existing requirements for sounding at the margins.

Index Terms—Firn, ice-penetrating radar, radar clutter, radar sounding.

I. INTRODUCTION

A IRBORNE radar sounding is the primary remote sensing modality for studying the englacial and subglacial conditions of polar ice sheets [1]. Applications range from

Manuscript received June 26, 2019; revised November 19, 2019; accepted February 4, 2020. The work of Riley Culberg was supported in part by the National Defense Science and Engineering Graduate Fellowship, in part by the NASA Cryospheric Sciences Program, and in part by the NSF CAREER Award. The work of Dustin M. Schroeder was supported in part by the NASA Cryospheric Sciences Program and in part by the NSF CAREER Award. (Corresponding author: Riley Culberg.)

Riley Culberg is with the Department of Electrical Engineering, Stanford University, Stanford, CA 94305 USA (e-mail: culberg@stanford.edu).

Dustin M. Schroeder is with the Department of Geophysics, Stanford University, Stanford, CA 94350 USA, and also, by courtesy, with the Department of Electrical Engineering, Stanford University, Stanford, CA 94350 USA (e-mail: dustin.m.schroeder@stanford.edu).

Color versions of one or more of the figures in this article are available online at http://ieeexplore.ieee.org.

Digital Object Identifier 10.1109/TGRS.2020.2976666

mapping ice thickness and subglacial topography [2], [3] to studies of glacial hydrology [4], [5] and basal thermal regimes [6]. These observations provide foundational data and boundary conditions on the current mass balance of the polar ice sheets and feed numerical ice dynamics models developed to predict their future response to climate change and the associated sea-level contribution [7]. Unfortunately, despite extensive surveys of both Antarctica and Greenland over the last 30 years, significant impediments to multidecadal, continental-scale studies remain. Pritchard [8] identified over 500 000 km² of Antarctica that have never been surveyed, and the existing data record spans well in the excess of 35 surveys from more than eight airborne radar instruments-all with different system and processing parameters [3]. Rignot et al. [9] found a 2%-15% uncertainty in current ice discharge rates for the continent due to this incomplete ice thickness information alone, and data heterogeneity has significantly limited largescale studies [10]. Pritchard [8] also identified community requirements for improved temporal coverage in the most dynamic regions of the ice sheets. These requirements point toward a need for new platforms, which can offer stable, repeatable data collection with wide spatial coverage and high revisit rates. A satellite radar sounder would be one such potential platform.

Orbital radar sounding of the Martian polar ice caps has been successfully demonstrated by both the Mars Advanced Radar for Subsurface and Ionosphere Sounding (MARSIS) [11] and the Shallow Radar (SHARAD) [12] instruments. Operating at center frequencies between 1 and 5 MHz, MARSIS detected basal reflections through ice up to 3.2 km thick in the South Polar Layered Deposits [11], comparable with terrestrial airborne sounders that sound ice up to 4 km thick on Earth [13]. SHARAD operates at 20 MHz and has a more limited penetration depth of 1500 m [14], but the commensurate improvement in the bandwidth permits the clear resolution of stratigraphic layers, which have been used to infer the history of climate-driven accumulation and erosion in the North Polar Layered Deposits [15]. Building on these successes, both the United States and European space agencies will include high-frequency (HF) and/or very HF (VHF) sounding instruments on upcoming missions to the icy Jovian satellites [16], [17].

Altogether, this suggests that many of the engineering hurdles to an orbital radar sounding instrument for terrestrial polar science are surmountable. However, both

0196-2892 © 2020 IEEE. Personal use is permitted, but republication/redistribution requires IEEE permission. See https://www.ieee.org/publications/rights/index.html for more information.

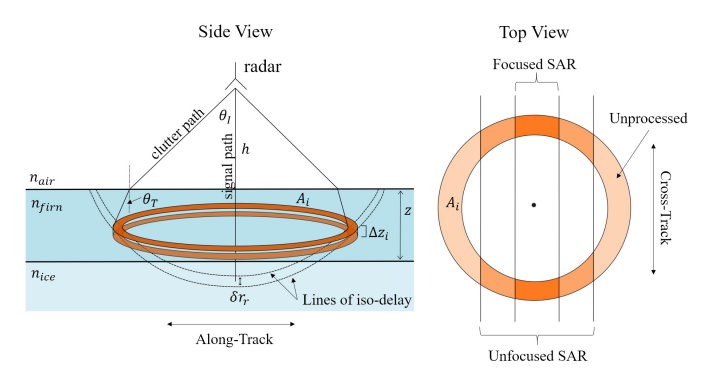


Fig. 1. Radar sounding geometry. The power measured in a given range bin is the superposition of backscatter from all dielectric interfaces or inhomogeneities between the two dashed curves. Backscatter at any given depth is a function of the orange illuminated area. Unfocused or focused SAR processing shrinks this area by narrowing the effective along-track beamwidth.

the Earth's ionosphere and International Telecommunications Union (ITU) spectrum allocations for Earth-observing satellites significantly limit the choice of the system center frequency and bandwidth. MARSIS and SHARAD are both HF instruments, and the majority of airborne radar sounders operate in the VHF band between 60 and 200 MHz [18]. In contrast, the most attractive existing satellite allocation is centered at 435 MHz [19] although some studies have also considered 45 MHz [20]. As a result, evaluating high-altitude sounder performance across a range of frequencies, including the ultrahigh-frequency (UHF) band, is critical to assessing the feasibility of terrestrial orbital radar sounding.

Both theoretical and experimental studies have identified surface clutter as a significant impediment to high altitude and UHF sounding [21]-[23]. Due to the broad beamwidths of sounding antennas, off-nadir scattered returns from the surface can experience the same two-way travel time and, thus, interfere with nadir reflections from the subsurface (see Fig. 1). As the surface signal is not subject to englacial attenuation, it is typically much stronger than the nadir signal and can mask true subsurface features in the radargram [24]. In the along-track direction, synthetic aperture radar (SAR) processing can effectively migrate power to the appropriate depth [2]. However, cross-track scatterers experience the same time delay and Doppler shift as the nadir reflection, making the returns ambiguous. Clutter tends to increase with sounding frequency as the surface roughness relative to the illuminating wavelength also increases, resulting in greater off-nadir scattering [25]. In addition, as altitude increases, the angle of illumination for clutter cells decreases. For typical scattering behavior, this corresponds to increased clutter power [26]. As a result, surface clutter models have received extensive treatment in both the airborne and planetary sounding literature [22], [27], [28].

More recently, analysis of data from POLarimetric Airborne Radar Ice Sounder (POLARIS), a 435-MHz airborne testbed radar, raised the possibility that scattering in the near-surface polar firn may be a constraining source of clutter. Dall [29] found that nearly all data collected by this system displayed strong echoes in the top 100–200 m of the ice column, which were not believed to be present in VHF sounding data.

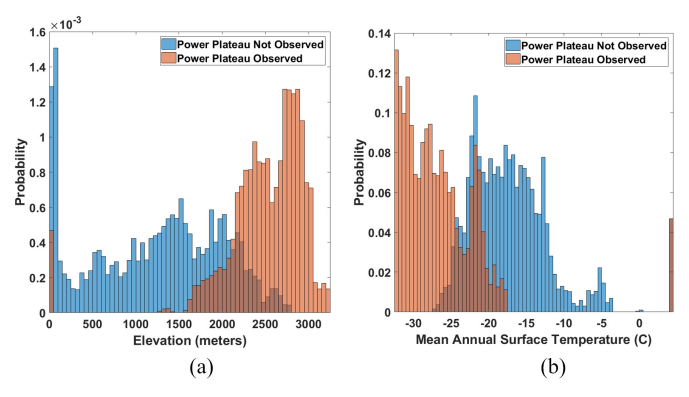


Fig. 2. (a) Elevation and (b) mean annual surface temperature statistics of regions in Greenland where the near-surface power plateau is observed (orange) or not observed (blue) in AR transects. Based on the principle of maximum likelihood, we identify thresholds of surface elevation orgeater than 2100 m or surface temperature below -24 °C for classifying other areas likely to exhibit this behavior.

Using empirically-derived backscatter coefficients and angular scattering functions, they showed that for an orbital sounder, either thermal noise, surface clutter, or firn clutter could prevent the detection of the bed over the majority of Antarctica [30]. However, as noted by the authors, this result heavily depends on the assumption that the firn should be treated as a volume scattering medium. The projected signal-to-clutter ratio (SCR) would be greatly improved if the dominant scattering mechanism was instead quasi-specular reflection [30]. This question on the nature of radar scattering in polar firn remains open. In addition, due to the empirical basis of the POLARIS studies, it was not possible to project the performance of instruments with different system parameters from that testbed.

The spatial and spectral prevalence of this near-surface "power plateau" first identified in the Antarctic POLARIS data suggests that these are critical gaps to address. We conducted a preliminary manual review over 15 600 km of trans-continental flight transects collected in Greenland by the University of Kansas Center for the Remote Sensing of Ice Sheets (CReSIS) Accumulation Radar (AR), the only other operational UHF airborne radar sounder, to determine if a near-surface power plateau was evident. Radar traces were considered to show a power plateau if the gradient of the smoothed trace was near-zero or nonnegative over some depth intervals of more than 10 m. We compared the surface elevation, mean annual accumulation, and mean annual surface temperature statistics of the regions with and without this power plateau and found both surface elevation and mean annual surface temperature to be good predictors for the presence of this scattering behavior (see Fig. 2). Based on the principle of maximum likelihood, we identified surface elevations above 2100 m, or mean annual surface temperatures below -24 °C, as thresholds for the presence of this power plateau. In addition, we reviewed coincident VHF radar collections on the same flight transects and identified clear power plateaus in the same regions, suggesting that this clutter mechanism may be a concern regardless of sounding frequency (examples in Fig. 3). Based on the identified elevation and surface temperature thresholds, we conservatively estimate that this firn scattering feature is

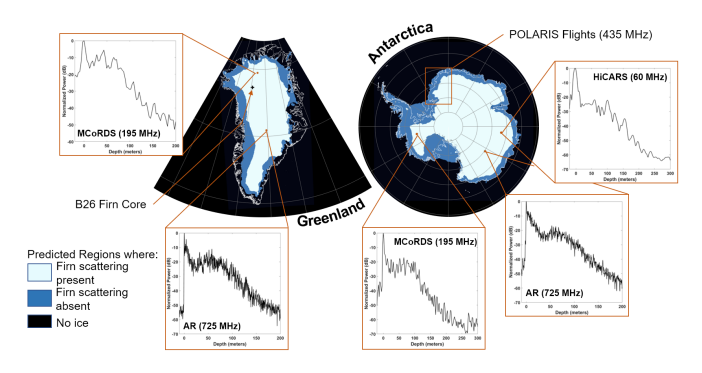


Fig. 3. Spatial prevalence of elevated near-surface radar returns in both Greenland and Antarctica with representative depth-power profiles. Systems include the CReSIS AR and MCoRDS3 Depth Sounder and the University of Texas HiCARS2 instrument. The near-surface power plateau is clearly evident across a wide range of systems, center frequencies, and locations.

present in at least 65% of the ice-covered area of both Antarctica and Greenland. Clearly, if these bright near-surface returns produce deep clutter in high-altitude acquisition geometries, they could present a serious impediment to the feasibility and performance of terrestrial orbital radar sounding. Therefore, in this article, we investigate the following questions.

- 1) What is the dominant radar scattering mechanism in the polar firn in the VHF and UHF bands?
- 2) What is the frequency, bandwidth, and altitude dependence of any clutter resulting from this mechanism?
- 3) Does this mechanism constrain the ability of an orbital radar sounder to detect the bed beneath the continental ice sheets?

Section II describes the processing methods and data used for model validation. In Section III, we then introduce the physical models of polar firn that lay the groundwork for the analytic electromagnetic models we develop and test in Section IV. In Section VI, we apply the best fit model to evaluate the frequency, bandwidth, and altitude dependence of firn clutter power. Section VII discusses the implications of that behavior for an orbital radar sounder link budget.

II. DATA AND PROCESSING

To address the question of radar scattering mechanism, we use a unique study area in the high-elevation accumulation zone of Northwest Greenland, which includes both VHF and UHF radar transects in close proximity to the B26 firn core from the 1995 North Greenland Traverse. Gamma-ray attenuation density measurements were made on the firn core at a 1-mm sample spacing between 0.2 and 119.7 m depth [31]. This permits the direct comparison of *in situ* measurements of firn density with independent radar observations of the same area at multiple frequencies.

Both radar transects were collected by CReSIS—one in 2011 with the AR and another in 2014 with the Multichannel Coherent Radar Depth Sounder (MCoRDS3) [32], [33]. The full system details for the flight segments used in this article are presented in Table I.

To obtain radargrams and depth-power profiles, we pulse compress and power detect the raw data using the CReSIS

TABLE I RADAR SYSTEM PARAMETERS

Parameter	MCORDS3	Accumulation Radar	
Date and Segment	20140508_01_061	20110506_01_027	
Center Frequency	195 MHz [37]	725 MHz [37]	
Bandwidth	30 MHz [37]	320 MHz [37]	
Range Resolution in Firn	6 meters [37]	0.65 meters [37]	
Transmit Power	1050 W [38]	1.25 W [39]	
Mean Flight Altitude	470 m	460 m	
Raw PRF	12 kHz	50 kHz	
Hardware Presums	35	128	
Effective PRF	343 Hz	390 Hz	
Trace Spacing	0.41 meters	0.38 meters	
Mean Flight Velocity	144 m/s	148 m/s	
Antenna Along-Track Half-	~120 degrees [40]	~ 21 degrees [39]	
Power Beamwidth			
Distance to B26 Core	350 meters	910 meters	

Processing Toolbox [34], correct for geometric spreading and attenuation losses, and normalize to the surface reflection. The attenuation profile is calculated from the B26 conductivity profile following MacGregor *et al.* [35]. To estimate the off-nadir scattering behavior at a given depth in the firn, we treat the Doppler spectrum as an empirical estimate of the angular scattering function where the relationship between the Doppler frequency and the in-firn illumination angle is given in (1). The Doppler frequency is given by f_D , λ is the free space wavelength, v is the flight velocity, and v0 is the mean refractive index between the surface and the depth of interest

$$\theta_T = \sin^{-1}\left(\frac{f_D\lambda}{2vn_f}\right). \tag{1}$$

The Doppler spectrum is found by taking the fast Fourier transform (FFT) of an along-track aperture at each depth and incoherently averaging 100 apertures with a 90% overlap. For the MCoRDS3 data, we use an aperture approximately equal to the physical along-track half-power beamwidth of the radar, a distance of 1.4 km encompassing 3427 traces. This results in an average angular resolution of 0.039°. We choose the processing aperture for the AR such that the same angular resolution is achieved. This results in a processing aperture of approximately 300-m encompassing 816 traces. For this system, the processing aperture exceeds the physical alongtrack half-power beamwidth by approximately 7°. The spectrum is then range migrated in the frequency domain [36] and normalized to peak power. We do not correct for geometric spreading loss, as we account for this amplitude factor in our spectral models. To permit direct comparison of the spectra, despite the difference in range resolution, we average together all AR range bins within a given MCoRDS3 range bin. Radargrams were not corrected for surface topographic variations prior to Doppler spectrum processing.

After hardware presums, the effective beamwidth of the AR in the firn is approximately 22°, while the physical half-power beamwidth of the antenna array is only 14°. Similarly, the effective beamwidth of MCoRDS3 after presums is approximately 76° in firn, where the physical half-power beamwidth is 64°. To avoid the confounding effects of the

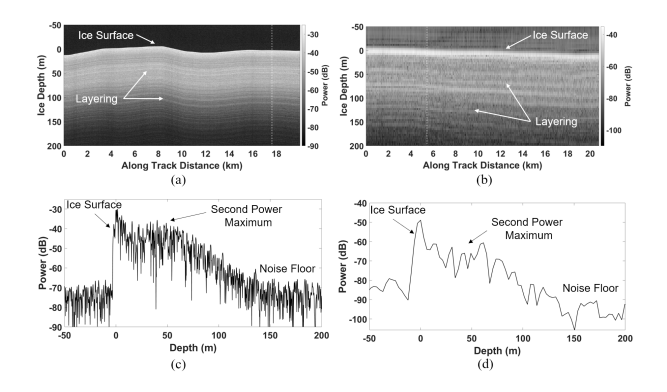


Fig. 4. (a) AR and (b) MCoRDS3 radargrams. The white dashed line shows the trace of the closest approach to the B26 firn core site. These traces are plotted for the (c) AR and (d) MCoRDS3.

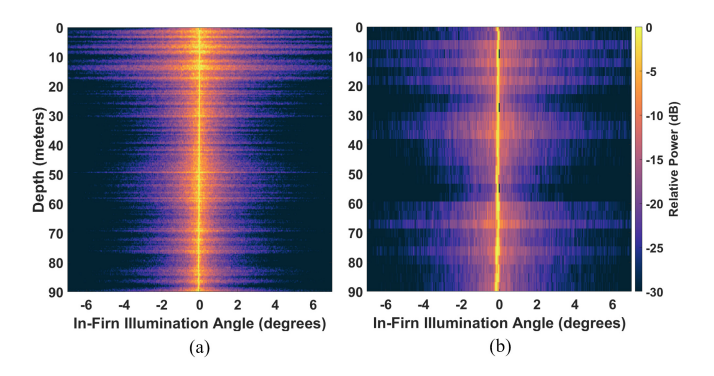


Fig. 5. (a) AR and (b) MCoRDS3 Doppler spectra, normalized to peak power in each range bin.

antenna pattern on the Doppler spectrum in the subsequent analyses, we restrict our analysis of the Doppler spectra to an angular range of -7 to 7° off-nadir.

From this empirical data set, we identify five key features, which a satisfactory model must be able to reproduce in order to explain the observed firn echo properties.

- The radargrams in both frequency bands show continuous horizontal layering in the upper 200 m of the ice sheet.
- 2) The depth-power profile in both frequency bands shows a distinct minimum at around 30 m depth, with the second maximum in power between 50 and 60 m, followed by rapid power decay.
- 3) The subsurface angular scattering function is sharply peaked at nadir and decays monotonically with increasing illumination angle, typically to at least 25 dB below peak power within the first 7°.
- 4) The subsurface angular scattering function in both frequency bands is less specular than the surface, but becomes increasingly specular with depth.
- 5) The angular scattering function is significantly more specular at 195 MHz than at 725 MHz and consistently shows a strong specular peak at near-zero Doppler.

Figs. 4 and 5 show examples of these features in the radargrams, depth-power profiles, and Doppler spectra of the analyzed radar data. While we directly consider a very small data set due to the lack of high-resolution firn core data collocated with UHF and VHF radar transects, features 1–4 are present in the original Antarctic POLARIS data [30] and are consistent with features we observe in data from across the high-elevation accumulation zones of both Antarctic and Greenland (see Fig. 3).

III. PHYSICAL MODELS OF POLAR FIRN

Before discussing plausible electromagnetic models, it is useful to review the physical models of polar firn on which they are based. Since the observed scattering behavior is predominately present in regions of low surface temperature, we restrict our consideration to dry firn and do not consider the effects of surface melt or percolation and refreeze features [41].

Side-looking SAR and radar altimetry models, due to their viewing geometry and short wavelengths, typically treat firn as a volume scattering medium [42]–[44]. On the microscopic scale, firn consists of closely packed ice grains separated by air-filled pore space, which is evident in 3-D tomographic scans of firn cores [45]. Typical pore sizes range from the submillimeter to 1-cm scale [46], [47]. As the firn undergoes compaction with depth, this pore space is reduced. Therefore, the depth-density profile can be viewed as a continuous change in porosity, which alters the number of scatterers contributing to the observed radar return.

By contrast, in radar sounding studies, the dry firn is treated as a stratified medium, consisting of discrete layers deposited on a seasonal basis, which vary in density and permittivity. Fujita *et al.* [48] demonstrated that reflecting horizons in the ice column shallower than 1000 m could reasonably be attributed to changes in density. Similarly, Lewis *et al.* [49] showed a strong correlation between the trend in the standard deviation of ice core density measurements and the relative magnitude of layer reflection coefficients derived from AR surveys. On a regional scale, high-resolution radar systems designed to investigate the near surface have shown clear evidence of continuous layering over horizontal scales of many kilometers in both Antarctica and Greenland [49]–[51].

However, on a local scale, firn-core and snow trench studies demonstrate that there is significant horizontal variation in density due to spatial variability in deposition and compaction patterns. In the first meters of the firn, these variations manifest as regular discontinuities in the higher density layers [52], [53]. At greater depth, a series of adjacent deep firn cores in Queen Maud Land, Antarctica shows an almost complete loss of correlation in the density profiles for cores separated by as little as 13 m [54], further supporting a laterally rough or inhomogeneous firn model.

IV. ELECTROMAGNETIC MODELS OF POLAR FIRN

Based on the physical models of polar firn discussed in Section III, we consider the following mechanisms, shown in Fig. 6, for the observed near-surface radar returns:

- 1) off-nadir surface clutter migration to the subsurface;
- 2) volume scattering from air-filled pore space or density inhomogeneities in the firn;

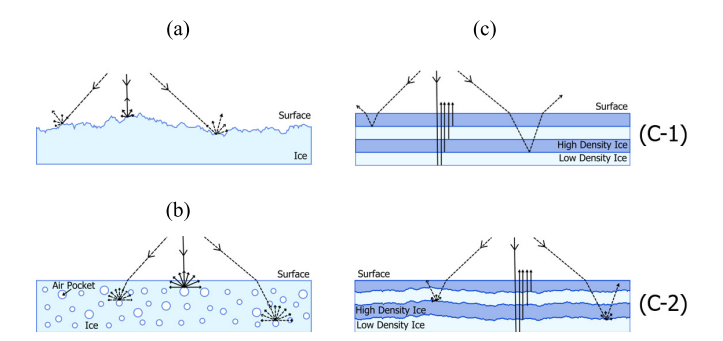


Fig. 6. Electromagnetic models of radar scattering in polar firn. Black solid lines indicate the signal path, and black dashed lines show example clutter paths. (a) Surface clutter: A surface produces some backscatter at off-nadir angles, which arrives at the radar at the same time as subsurface reflections due to the longer path length. (b) Volume scattering: Individual air pockets or density inhomogeneities within the firn scatter isotropically, and the radar receives the incoherent sum of the power backscattered from each pocket in the illuminated area. (c) Quasi-specular reflection. (C-1) Layers of varying density within the firn act as perfectly specular thin-film reflectors and return no energy at off-nadir angles of illumination. (C-2) Some scattered power is returned at off-nadir angles of illumination due to the small-scale roughness in the horizontal profiles of iso-density.

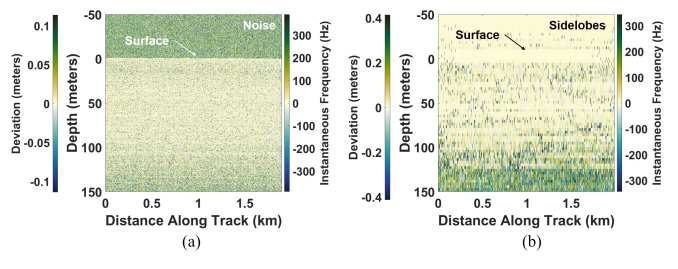


Fig. 7. Instantaneous frequency and height deviation of near-surface layers from the along-track phase gradient of the (a) AR and (b) MCoRDS3 transects.

- 3) quasi-specular reflections at the interface between the layers of different densities with the Doppler spectrum controlled by one of the following:
 - a) propagation of phase and amplitude errors;
 - off-nadir scattering from slightly rough iso-density interfaces.

A. Surface Clutter

Under this model, the observed subsurface power plateau would be the result of off-nadir surface scattering mapping to the subsurface, rather than scattering from the firn itself. However, we find that this model fails to account for the trends seen in the empirical data. First, if the near-surface power was dominated by incoherent clutter, we would not expect to see any structure in the radargrams. However, clear horizontal layering is evident in both (Fig. 4). Second, we analyze the along-track phase gradient [55] of the near surface and find that it is tightly distributed around zero Doppler (Fig. 7). If the power was primarily attributable to migrated clutter, the distribution would be shifted to the Doppler frequency of the appropriate scattering angle. Therefore, the observed power is likely due to scattering from subsurface features, rather than superimposed surface clutter.

B. Volume Scattering

If the firn acts primarily as a volume scattering medium [43], the power received by the radar is proportional to the sum of the energy backscattered by each air-filled pore in the illuminated ice volume. As shown in Fig. 1, in the absence of any processing, this illuminated volume is a bowl containing every point with an equivalent optical path length as the subnadir point. Appendix A describes in detail how we compute this geometry. The scattering process within this volume is inherently incoherent, resulting in geometric spreading losses proportional to the inverse fourth power of range and producing an isotropic angular scattering pattern. Appendix B derives the volumetric radar cross section and extinction coefficients which, substituted into our geometric model, give the discrete approximation to the volumetric radar equation shown in (2). Here, P_R is the power received by the radar, P_T is the peak transmit power, G is the antenna gain, T is the transmission loss through the ice surface, λ is the free space wavelength, h is the platform altitude, z is the depth of interest, n_f is the refractive index of firn, $\sigma_b(r, \epsilon)$ is the radar cross section of a single scatterer as a function of radius and permittivity, A_i is the illuminated area at a given layer, ϕ_i is the porosity of the layer, ξ_a is the absorption efficiency, and ξ_s is the scattering efficiency. We have discretized the firn pack into M layers each of thickness Δz

$$\frac{P_T G^2 T^2 \lambda^2}{(4\pi)^3 n_f^2 \left(h + \frac{z}{n_f}\right)^4} \sigma_b (r, \epsilon)
\times \left\{ \sum_{i=1}^M A_i \Delta z_i \phi_i \left(\frac{3}{4\pi r^3}\right)
* \exp\left[-2\sum_{j=1}^i \Delta z_j \phi_j \left(\frac{3}{4\pi r}\right) \left[\xi_a (r, \epsilon) + \xi_s (r, \epsilon)\right] \right] \right\}.$$
(2)

For this mechanism, we model the pore radar cross section, absorption efficiency, and scattering efficiency using Mie theory [44], where the background medium is pure ice with a permittivity of 3.17 and the inclusions are air with a permittivity of 1. The porosity of a given layer is derived from the average depth-density profile of the B26 ice core over the discrete layer thickness relative to the density of glacial ice (917 kg/m³). Although some coherent summations have been applied to our data, the effective beamwidth after hardware presums is larger than physical half-power beamwidth for both systems, so for this analysis, we assume that the illuminated ice volume is not altered by processing.

Since this model estimates absolute power, the radar data must be absolutely calibrated before comparison. To do so, we assume that the surface is a quasi-specular reflector with some root-mean-square (rms) height, σ , calculated from Airborne Topographic Mapper (ATM) lidar collected coincident with the radar data [56], [57]. Then, the absolute power of the surface return is given in (3), where $|\Gamma|^2$ is the Fresnel reflection coefficient, k is the wavenumber, and N is the number of hardware presums applied to the data [58]

$$P_R(0) = \frac{NP_T G^2 \lambda^2 |\Gamma|^2}{(4\pi)^2 (2h)^2} \exp[-(2k\sigma)^2].$$
 (3)

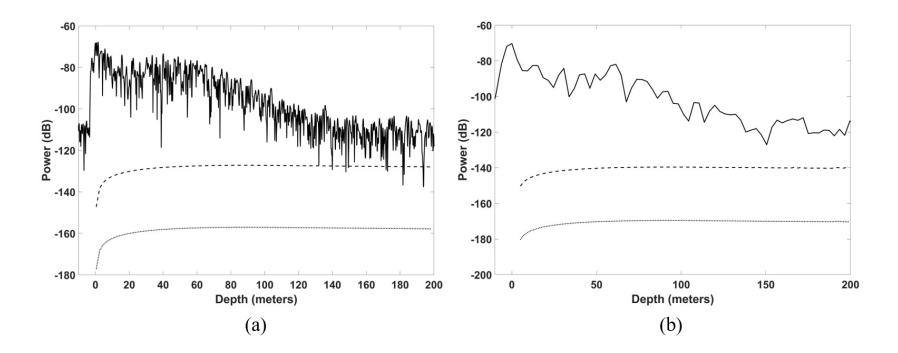


Fig. 8. Simulated power from firn volume scattering compared with depth-power profiles from (a) AR and (b) MCoRDS3. Dashed and dotted lines show predicted power for mean pore radii of 1 cm and 1 mm, respectively.

We conduct a parameter sweep over a range of physically plausible pore radii from 1 mm to 1 cm [47], [59] at 1-mm increments and compute the mean square error between the modeled and observed depth-power profiles in each frequency band. As $r \ll k$ for both systems, scattering is confined to the Rayleigh regime, and as expected, we find a monotonic increase in backscattered power as pore radius increases. However, due to the small pore size relative to the illuminating wavelengths, geometric spreading losses proportional to the inverse fourth power of range [44], and the low dielectric contrast between air and glacial ice, volume scattered power is at least 40 dB below the surface return in both frequency bands. In contrast, the second power maximum observed in the data is typically 10-15 dB below the surface return (see Fig. 8). In addition, this model fails to predict horizontal layering and cannot reproduce the sharp power decay observed below 60 m depth.

To understand if the observed power plateau could ever be produced by volume scattering, we conduct a further parameter sweep of radii from 1 cm to 0.5 m. The closest, although still poor, fit to the data is achieved for a radius of 0.4 m. For inhomogeneities beyond this size, the backscattered power decreases again due to high absorption and scattering losses in the firn. Regardless, near meter-scale air-filled voids in the firn are unobserved and physically unlikely. Density inhomogeneities of this size might be plausible, particularly in the case of refreeze features in percolation zones. The presence of any water or brine in the firn pore space would also significantly alter these results and might make volume scattering a more plausible mechanism in regions of significant surface melt, crevassing, or on ice shelves. However, in dry polar firn, volume scattering seems unlikely to account for the observed power plateau.

As further confirmation, we compare the angular scattering function of a volume scattering medium to the observed Doppler spectra. The radar cross section is isotropic; therefore, the only contributors to angular decay are the radar antenna beam pattern and the increasing distance to the scattering voxel with angle. As we limit our analysis to angles between -7° and 7° , neither factor contributes significantly in this analysis and the modeled angular scattering behavior is effectively independent of the observation angle. However, the observed angular scattering patterns decay rapidly with an

increasing angle (Fig. 5). Therefore, we assess that in the dry snow zone, volume scattering cannot account for the bright firn returns observed in both VHF and UHF airborne radar data.

C. Quasi-Specular Reflections

If, instead, firn is predominately a stratified medium, the observed subsurface power profile is produced by the interference of quasi-specular reflections at interfaces between layers of different densities [49]. To test this hypothesis, we employ a 1-D layered dielectric medium model where the permittivity of each layer is directly proportional to its density following the empirical relationship in (4) where ρ is the layer density in g/cm³ [60]:

$$\epsilon' = (1 + 0.845\rho)^2. \tag{4}$$

The layer thickness is set by the sampling interval of the B26 density profile. We neglect the imaginary component of the dielectric constant, as the dielectric contrast from conductivity changes is negligible compared to that induced by density changes in the firn [48].

The depth over which significant constructive or destructive interference among secondary reflections can occur is approximately equal to the system range resolution in firn [61]. Therefore, we estimate the effective reflection coefficient for each range bin by applying the transfer matrix method [62] to the stack of layers in each range bin, setting the half-space above the bin to the permittivity of the last layer in the previous range bin and the half-space below the bin to the permittivity of the first layer in the next range bin.

This model successfully reproduces the magnitude and trend of the depth-power profile in both frequency bands using only the B26 high-resolution density measurements and radar system frequency and bandwidth parameters as inputs to the model (see Fig. 9). It also predicts clear horizontal layering in the firn. We conclude that at nadir, the dominant radar scattering mechanism in dry polar firn is likely coherent quasi-specular reflections at interfaces of variable density. However, a 1-D model cannot address the angular scattering behavior evident in the empirical Doppler spectra. Therefore, we also consider modifications to this model, which are still consistent with a power profile dominated by coherent reflection

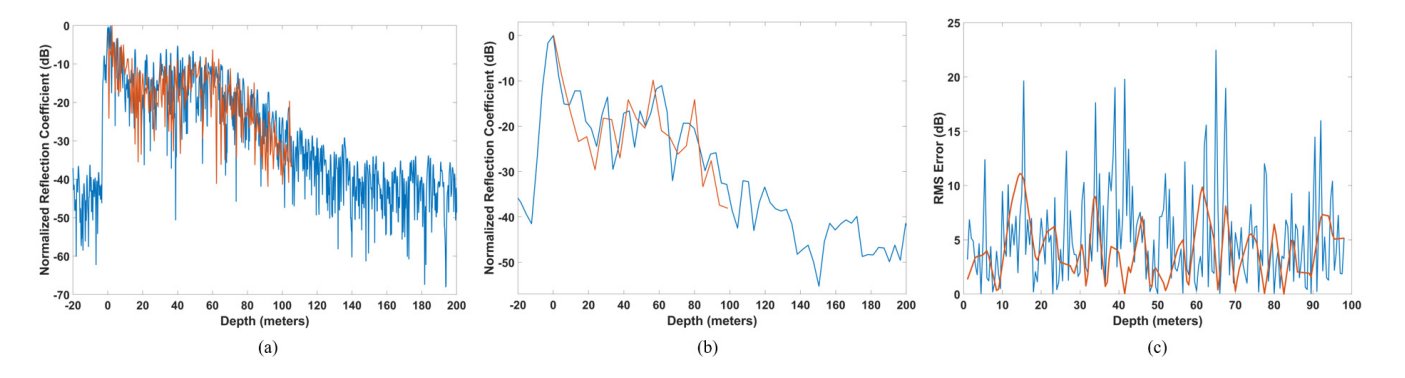


Fig. 9. Empirical data (in blue) compared with simulations (in orange). Depth-power profile from the (a) AR and (b) MCoRDS3 are compared to simulated reflection coefficients from the 1-D layered dielectric model (Section IV-C). (c) rms error between simulation and observation as a function of depth, where the blue curve is AR error and the orange curve is MCoRDS3 error.

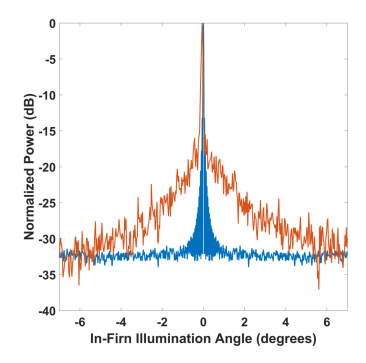


Fig. 10. Comparison of the AR Doppler spectrum at 55 m depth (orange curve) with the ideal response (blue curve) from a specular surface with a 10% additive amplitude noise in the time domain.

at normal incidence but include some off-nadir scattering mechanisms.

1) Doppler Spectrum Errors: It is possible that only specular reflection occurs in the firn, but the observed Doppler spectrum is broadened by random phase and amplitude errors between traces that propagate through the FFT. In addition, the width of the main lobe may be limited by the frequency resolution of the FFT. However, as shown in Fig. 10, we find that these errors fail to reproduce the observed spectra. At small angles, the spectrum is significantly wider than the ideal FFT response, indicating that this broadening is not solely the result of limited frequency resolution. Because the Fourier transform is linear and unitary, the addition of additive white Gaussian noise in the time domain can raise the noise floor in the frequency domain [63], but cannot reproduce the high power observed only at low frequencies. It is possible that some forms of multiplicative, colored, or non-Gaussian noise affect the spectrum, but given the consistency in the power trend across different systems and collection dates, we assess it is more likely that the observed spectra are the result of off-nadir scattering.

2) Rough Layers: For rough surfaces with rms heights less than a quarter wavelength, a strong coherent reflection component is present at normal incidence as observed, but some off-nadir scattering still occurs [25], [64]. It is, therefore, possible that the observed angular scattering behavior is the

result of small-scale roughness in the horizontal profile of isodensity layers. Snow trench studies indicate that topographic surface expression is lost through compaction in the upper 1–2 m of the firn [52], [53], and that draping over bed topography is unlikely close to the surface [65]. This, along with the specularity of the Doppler spectra and the tight distribution of the along-track phase gradient around zero in both radargrams, suggests that the subsurface layers may be well-modeled by relatively small perturbations to a flat plane. Therefore, we apply the simplified integral equation method (S-IEM) developed by Fung and Chen [66] to model the scattering behavior of the firn, under the assumption of negligible interference between layers due to incoherent scattering

This model assumes a statistically stationary scattering surface, which can be parameterized by some rms height, σ , and correlation length, L. The particular formulation used in this article neglects multiple scattering or shadowing and is, therefore, consider valid for $k\sigma < 2$ and an rms surface slope of less than 0.3 [66]. To remain within this region of validity, interface rms heights in firm should not exceed 30 cm for MCoRDS3 or 8 cm for the AR and the correlation length must be longer than 1.4 m and 30 cm, respectively. The surface rms heights measured from the coincident collection by the ATM lidar system fall between 4 and 7 cm [56], [57], which suggests that this model should be valid for our data.

The co-polarized radar cross section from the S-IEM model under these assumptions is given in (5). The full form of I is provided in Appendix C. Here, the subscript f denotes that we consider the wavenumber and illumination angle in the firn at the depth of interest, accounting for the variable index of refraction as calculated from the density profile

$$\sigma_s^0(\theta) = \frac{k_f^2}{4\pi} \exp[-2(k_f \sigma \cos \theta)^2] * \sum_{n=1}^{\infty} |I^n|^2 \frac{W^n (2k_f \sin \theta_f)}{n!}$$
(5)

W is the surface spectrum, which corresponds to the Fourier transform of the surface correlation function. For this analysis, we assume an exponential correlation function with W taking

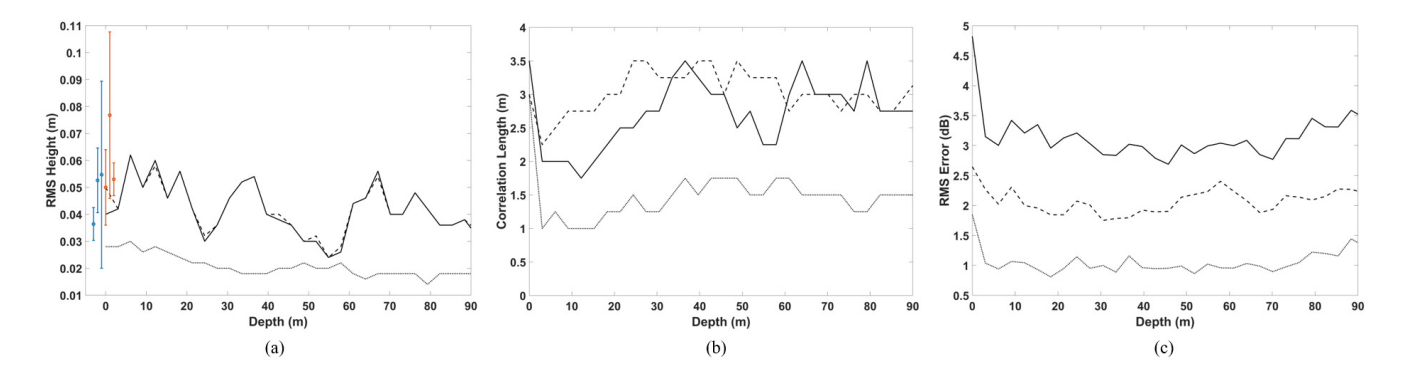


Fig. 11. Estimates of rms height and correlation length in each range bin from the rough layer inversion. Dotted curves show the results of the inversion of the AR data. Dashed curves show the results of the inversion of the MCoRDS3 data. Solid curves show the results of the joint inversion in both frequency bands. (a) Estimated rms height in each range bin. Red error bars show the range of surface rms heights measured over the MCoRDS3 transect from ArcticDEM, coincident ATM collection, and RSR inversion of the radar data. Blue error bars show the range of surface rms heights measured over the AR transect from the same three data sources. (b) Estimated correlation lengths. (c) rms error for each inversion.

the form given in the following equation:

$$W^{n}(2k_f \sin \theta_f) = \frac{2\pi nL^2}{[n^2 + (2k_f L \sin \theta_f)^2]^{1.5}}.$$
 (6)

The S-IEM model does not include the normal incidence coherent-reflected component. To derive this component, we use a similar approach to [67], starting from the radar cross section of a specular dielectric disk as defined in [68], assuming that the illuminated area is equal to the first Fresnel zone, and modifying it with the coherence loss function derived in [25]. Then, the radar cross section at normal incidence takes the form in (7), where $|\Gamma|^2$ is the Fresnel reflection coefficient at normal incidence

$$\sigma_c^0 = \frac{2\pi^2 \left(h + \frac{z}{n_f} \right) |\Gamma|^2}{\lambda_f} \exp[-(2k_f \sigma)^2].$$
 (7)

To evaluate this model, in each range bin, we invert for the rms heights and correlation lengths which separately minimize the mean square error between the modeled scattering behavior and the MCoRDS3 and AR data, as well as a single rms height and correlation length which jointly minimizes the mean square error between model and data in both frequency bands. This is achieved with a parameter sweep of rms heights between 5 mm and 8 cm, incrementing every 1 mm, and correlation lengths between 0.5 and 8 m, incrementing every 10 cm. Prior to calculating the mean square error, both the data and model output are normalized to their respective maximum values. Therefore, the model is constrained to fit the difference in power between the specular peak and scattered component, as well as the angular rate of the power decay, but not the absolute magnitude of the scattering coefficient.

If this model is representative of the radar scattering physics in firn, we expect the following behavior. First, the mean square error between the model and data should be small. Second, the individual and joint inversions should all produce similar estimates of rms height and correlation length. Finally, due to ongoing compaction and snow grain rearrangement, layer roughness should be on par with or less than surface roughness.

The results of the inversions are presented in Fig. 11. In addition, Fig. 12 shows the comparison of the spectra modeled from the jointly inverted rms heights and correlation lengths with the observed data. The rms error between data and model is very good in all cases. The estimated rms heights at the surface fall within the range of rms heights calculated from the coincident ATM data [56], [57], ArcticDEM [69], and radio statistical reconnaissance (RSR) inversion [64], [70] of the radar surface return. The trend in layer rms height behaves as anticipated, with rougher layers close to the surface and smoother layers at depth. The estimated correlation lengths also fall within physical plausible ranges. The greatest discrepancy in the result is the large difference in estimated rms height between the MCoRDS3 and AR inversion—roughly 5 cm versus 2.8 cm. However, there are a number of reasonable explanations. Most plausibly, the limited angular resolution of the FFT may prevent the resolution of the full height of the specular peak in the MCoRDS3 data. Only a 2-4-dB greater peak would be required to bring the MCoRDS3 rms height estimates in line with those from the AR. In addition, the larger bandwidth and wider cross-track beamwidth of the MCoRDS3 system likely contribute cross-track clutter to the spectrum, increasing the apparent scattered power and, therefore, the rms height.

To further validate this model, we simulate the expected SCR at the B26 site from 100 m depth to the bed and compare it to an estimate of the SCR derived from the MCoRDS3 data. Clutter is simulated using the geometry model described in Appendix A. We assume a firn depth of 90 m and calculated σ^0 at each layer using the S-IEM model. The rms height and correlation length are taken from the MCoRDS3 subsurface inversion. The reflection coefficient for each layer is calculated from the 1-D layered dielectric model described in this section. Given that the transmission coefficients of the firn layers are near unity and the total two-way attenuation through the firn layer is calculated from the B26 conductivity profile to be less than 3 dB; we neglect the attenuation term in the clutter model. We assume unfocused SAR processing with 35 coherent summations and model the MCoRDS3 cross-track beam pattern as the projection of a *jinc* pattern on to the surface in

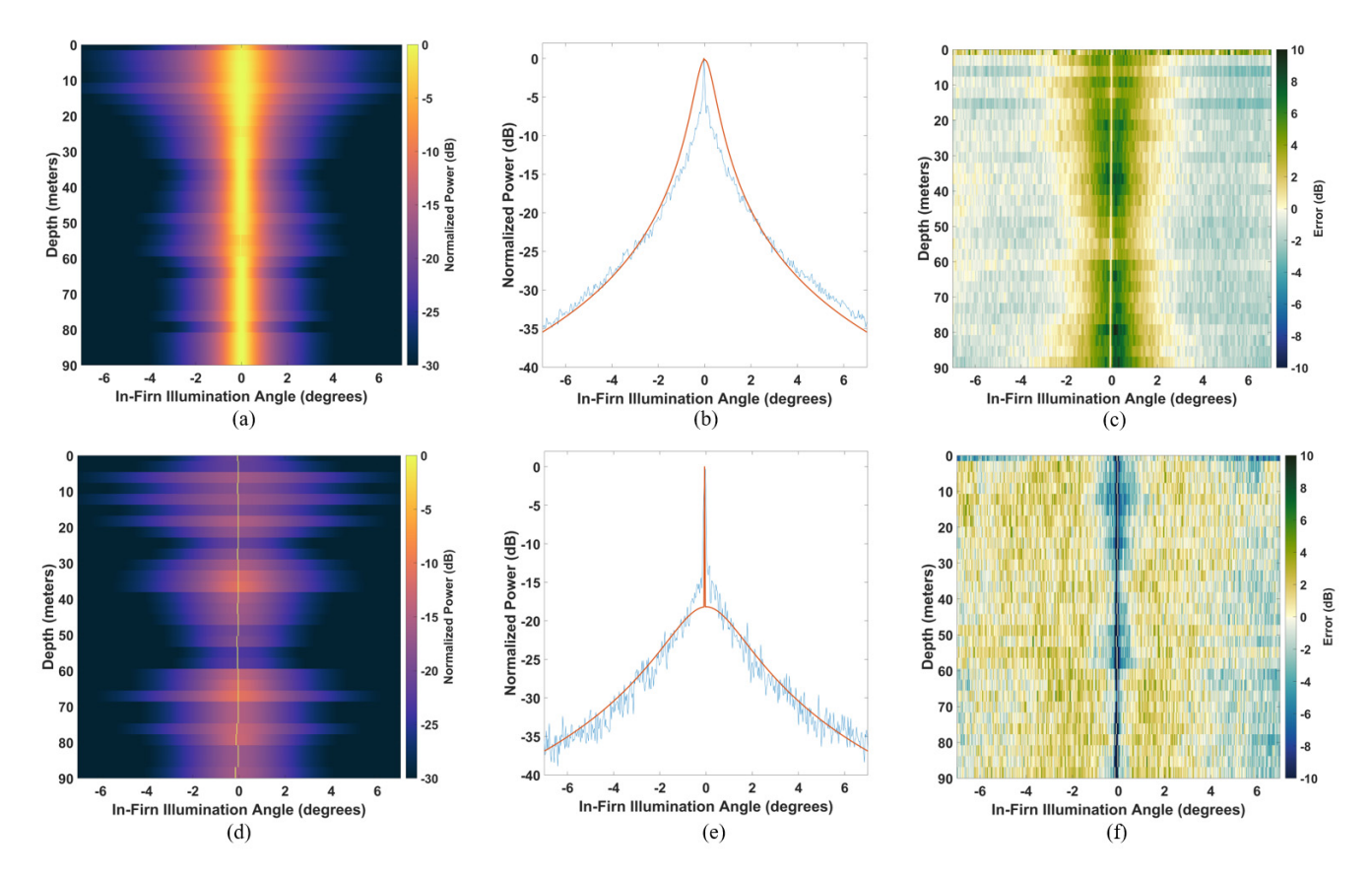


Fig. 12. Doppler spectra simulations with the S-IEM rough layer model. (a) Simulated AR Doppler spectra [compared to Fig. 5(a)]. (b) Example of the simulated (orange) and observed (blue) AR spectrum at 30 m depth. (c) Difference between simulated and observed AR spectra. (d) Simulated MCoRDS3 Doppler spectra [compared to Fig. 5(b)]. (e) Example of the simulated (orange) and observed (blue) MCoRDS3 spectrum at 30 m depth. (f) Difference between simulated and observed MCoRDS3 spectra.

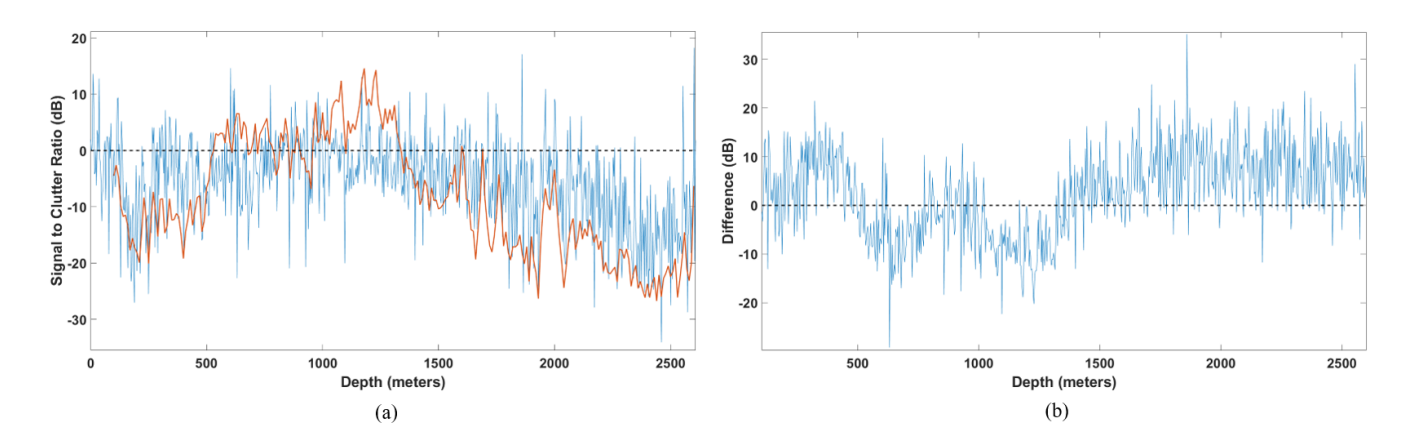


Fig. 13. (a) Comparison of the simulated (orange) and observed (blue) SCR as a function of depth in the MCoRDS3 radar data. Some of the discrepancies are likely due to inexact knowledge of the cross-track antenna beam pattern. (b) Difference between simulated and observed SCR. Negative numbers indicate an underestimation of clutter and positive numbers indicate overestimation.

the cross-track direction. The signal is taken to be the value of the calibrated, smoothed radar trace after 20 additional coherent summations. This automatically accounts for the appropriate reflection coefficients, geometric spreading loss, and attenuation through the ice column without requiring that we separately estimate those values. The empirical SCR is estimated to be the difference between a raw trace and a trace at the same location after 20 additional coherent summations

when both traces are normalized to their respective surface powers.

The results are presented in Fig. 13. We find very good agreement between model and data at depths above 1300 m, where cases of apparent underestimation are likely caused by regions where the signal is already greater than the clutter in the raw data, preventing a good estimate of observed SCR. Below 1300 m, our model consistently overpredicts clutter.

		MCoRDS3		Accumulation Radar		
Category	MODEL	Depth-Power Profile	Doppler Spectrum	Depth-Power Profile	Doppler Spectrum	Mean Square Error
Volume Scattering	1mm pore radius	6433 dB	754 dB	5401 dB	661 dB	8459 dB
-	1cm pore radius	2541 dB	754 dB	1929 dB	661 dB	3344 dB
	40cm pore radius	360 dB	754 dB	1459 dB	661 dB	1807 dB
Quasi-specular Layers	1D model	22.8 dB		46.9 dB		
	Spectral Noise		80.3 dB		186 dB	209 dB
	Rough Layers		5.04 dB		4.96 dB	52.6 dB

TABLE II
MEAN SQUARE ERROR OF OPTIMIZED MODELS

This is likely the result of discrepancies between our analytical approximation of the MCoRDS3 cross-track beam pattern and the true antenna pattern. Published analysis of the beam pattern only extends to 60° off-nadir [40], and at these depths, near-surface clutter is illuminated at angles above 70°. Given ground plane effects, the true antenna pattern likely decays more rapidly at large angles than our analytical approximation.

V. MODEL COMPARISON

As this article employs an inverse hypothesis testing approach to understand the radar scattering behavior of polar firn, we now compare the mean square error for each model. Table II provides a summary of these results. For each model, we calculate four error terms: the mean square error between the model and depth-power profile of each radar system from 0 to 90 m depth and the mean square error between the model and Doppler spectra of each radar system from 0 to 90 m depth and -7° to 7° along-track. We then sum these four terms in quadrature to give the total error listed in the right-most column of Table II.

While we cannot rule out all other hypotheses for the observed scattering behavior, we find that the quasi-specular layer model provides the best fit to the depth-power profiles and angular scattering functions in both frequency bands, given physically plausible model parameters. Therefore, we assess that of the mechanisms considered, the most plausible radar scattering mechanism in dry polar firn is a quasi-specular reflection at interfaces of variable density, with off-nadir scattering likely controlled by small-scale roughness in the iso-density profile produced by local spatial variability in topography, deposition patterns, and compaction rates.

VI. RADAR SYSTEM PARAMETER ANALYSIS

Having addressed the question of mechanism, we apply our best fit model to evaluate the frequency, bandwidth, and altitude dependence of both the firn power plateau and the clutter it produces.

To study the behavior of the plateau itself, we apply our 1-D layered dielectric model (Section IV-C) to depth-density profiles from six Greenland and Antarctic ice cores [31], [71]–[73]. The resultant profiles are highly similar, with some variations in firn depth and the prominence of the plateau. We take the ensemble average of these simulated reflection coefficients to be representative of the average

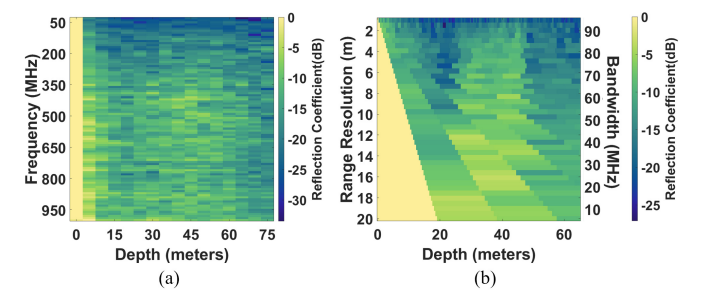


Fig. 14. Simulated firn layer reflection coefficients normalized to the surface reflection. Each plot shows the ensemble average of simulation runs using the 1-D layered dielectric model applied to depth-density profiles from six Antarctic and Greenland ice cores [31], [71]–[73]. Each row is analogous to a depth-power profile such as those shown in Fig. 10(a) and (b) and the power plateau is evident as the bright region centered around 45 m depth. (a) How the depth-power profiles changes as the system center frequency increases. Bandwidth is held constant at 30 MHz. The power plateau becomes increasingly bright and well-defined at higher frequencies. (b) Change in the depth-power profile for different system bandwidths at a constant frequency of 435 MHz. As the bandwidth decreases and range resolutions grow larger, the power plateau is both brighter and encompasses a greater range of depths.

response of polar firn. Our results show that the magnitudes of the firn layer reflection coefficients in the power plateau increase as the system center frequency is increased or bandwidth is decreased (Fig. 14). As a result, it is possible to partially mitigate this increase in the reflection coefficient with increasing center frequency by employing wider bandwidths. We find that below 80 MHz, the power plateau is generally at least 25 dB below the ideal surface reflections for bandwidths above 5 MHz. Between 80 and 200 MHz, the power plateau can still be kept below this threshold without increasing the system fractional bandwidth beyond 50%. Above 250 MHz, this mitigation is no longer possible, requiring fractional bandwidths above 100%. Therefore, the simplest means to limit the absolute power of firn echoes is to employ sounding frequencies below 80 MHz.

To examine the frequency, bandwidth, and altitude dependence of the total near-surface clutter, we calculate the expected clutter radar cross section at a depth of 2600 m, the mean ice thickness in the region where this behavior is prevalent. We define the clutter radar cross section as follows:

$$\sigma_{nsc} = \sum_{i=1}^{M} \Delta z_i A_i \sigma_i^0(\Gamma_i, \sigma_i, L_i, \lambda_f, \theta_i).$$
 (8)

The illuminated area, A, is calculated as described in Appendix A. We calculate the normalized radar cross

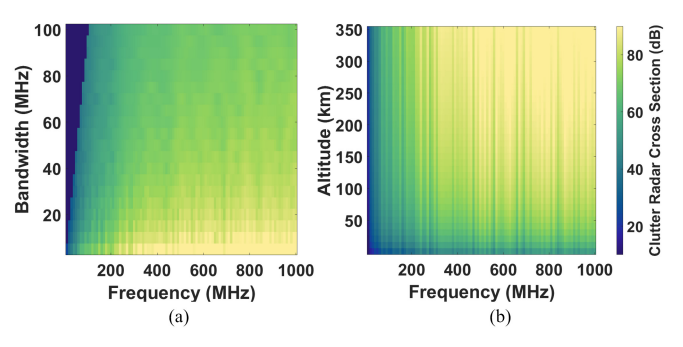


Fig. 15. Simulated clutter radar cross section at a depth of 2600 m. Each plot is simulated from the layer rms heights and correlations lengths estimated by joint inversion of the MCoRDS and AR Doppler spectra, applied in the S-IEM scattering model. (a) How clutter magnitude changes with frequency and bandwidth (range resolution). Altitude is held constant at 600 km. (b) How the clutter magnitude changes with frequency and altitude. Bandwidth is held constant at 6 MHz. The small-scale variations with frequency are the result of variations in the layer reflection coefficients due to thin-film interference within range bins.

section, σ^0 , from the S-IEM model using the rms heights and correlations lengths derived from joint inversion of the radar data and the Fresnel reflection coefficients calculated from the 1-D layered dielectric model.

Fig. 15(a) shows the clutter radar cross section for a range of frequencies and bandwidths at a fixed altitude of 600 km. The total magnitude of the clutter is greatest at high frequencies and low bandwidths, consistent with increased off-nadir scattering due to the large rms heights relative to the wavelength, and a large illuminated area contributing to the clutter power. (Note that the oscillations in the clutter power as a function of frequency are due to variations in the layer reflection coefficients from thin-film interference.) These results make it clear that increasing bandwidth to offset an increase in the frequency is most effective in the HF and VHF bands.

Fig. 15(b) shows the clutter radar cross section for a range of frequencies and altitudes at a fixed bandwidth of 6 MHz. We find a significant increase in clutter power with increasing frequency and increasing altitude. This behavior is intimately tied to the surface correlation length. Assuming a fixed surface correlation length, then at low frequencies, the correlation length is quite short relative to the wavelength and the scattered power is nearly constant across all illumination angles. Therefore, as the platform increases in altitude and clutter cells move from being illuminated at angles of around 30° to angles around 3°, the increase in the backscattered power is only a few dB. On the other hand, at higher frequencies, the correlation length is long compared to the wavelength, and scattered power peaks near nadir with a more rapid falloff with increasing angle. The change in illumination angle with platform altitude can then result in an increase in the backscattered power of nearly 30 dB. Altogether, these results suggest that for a fixed-bandwidth orbital sounder, HF or lower VHF center frequencies will always be most effective in suppressing this type of near-surface clutter.

Although our analysis in Section IV-B clearly demonstrated that volume scattering cannot account for the firn power plateau seen in airborne radar data, we consider the possibility that volume scattering from density inhomogeneities might contribute significantly to the total clutter budget in an

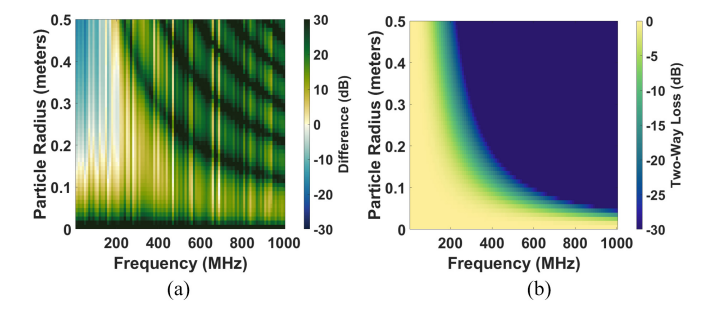


Fig. 16. Volume scattering metrics as a function of frequency and inhomogeneity size. In dry polar firn, the particle radius is generally less than a few centimeters. Larger radii might be possible in percolation zones or planetary settings. (a) Comparison of the difference between rough layer clutter and volume scattering clutter at 2600 m depth, 600 km altitude, and a bandwidth of 6 MHz. Positive numbers indicate that roughness clutter dominates, where negative numbers indicate that volume clutter is greater. (b) Total two-way attenuation through the firn column due to volume scattering. The color scale has been saturated at 30 dB of loss.

orbital geometry. We model the volumetric clutter radar cross section at a depth of 2600 m, altitude of 600 km, and bandwidth of 6 MHz for a range of frequencies and inhomogeneity sizes. The density contrast is assumed to be 50 kg/m³ with a fractional volume of 30%. Fig. 16(a) shows that under these conditions, rough interface scattering will almost always be the dominant clutter source, with the exception of sounding meter scale inhomogeneities frequencies in the HF band. More importantly, Fig. 16(b), which shows the total two-way loss through the firn column for these scenarios, demonstrates that in almost any volume scattering scenario which might produce noticeable clutter, the accompanying attenuation is the dominant effect. Our results suggest that in the dry polar firn, volume scattering is not a constraining factor for sounding even in the low GHz range, but that inhomogeneities on the scale of a few tens of centimeters could rapidly produce prohibitive losses in the firn column for UHF sounders.

VII. LINK BUDGET ANALYSIS

Of course, for practical system design, the SCR is the metric of greatest interest. Here, we conduct a basic link budget analysis to compare the performance of 45- and 435-MHz sounders in terms of SCR and signal-to-noise ratio (SNR) for a range of bed depths and reflection coefficients. The radar system and englacial parameters are presented in Table III. We assume that the subglacial interface can be treated as a quasi-specular reflector and apply (9) to calculate the signal power, on the basis of studies which suggest that even small coherent facets within the illuminated footprint are sufficient to maintain a geometric fall-off rate proportional to the inverse square of range [67], [74]. Here, $L_{\rm ice}$ is the englacial attenuation

$$P_{S} = \frac{P_{T} G^{2} \lambda^{2} T^{2} L_{\text{ice}}^{2} |\Gamma|^{2}}{(4\pi)^{2} \left[2 \left(h + \frac{d}{n_{\text{ice}}} \right) \right]^{2}}.$$
 (9)

Peters *et al.* [58] give bed reflection coefficients between -6 dB for a thawed till bed and -33 dB for a frozen bedrock bed. We extend this range by -20 dB to account

TABLE III
LINK BUDGET PARAMETERS

Parameter	Value
Center Frequency	45 MHz, 435 MHz
Bandwidth	6 MHz
Transmit Power	100 W
Antenna Gain	Isotropic − 0 dB
	Array – 16 dB
Altitude	600 km
Pulse Length	85 μs
Pulse Repetition Frequency	242 Hz
Velocity	7562 m/s
Attenuation Rate	10.7 dB/km
$ \Gamma ^2$ Range	-85 dB to -6 dB
Depth Range	1000-4000 m

for some roughness loss. We also consider the detectability of deep internal layers, using reflection coefficients between -80 and -65 dB based on [75]. The englacial attenuation rate is taken to be 10.7 dB/km following Matsuoka *et al.* [76]. We assume a plausible peak transmit power of 100 W for a high technical readiness level system [77] and a platform altitude of 600 km. Noise power is calculated using the form in (10), where K is Boltzmann's constant, β is the system bandwidth, $T_{\rm ant}$ is the antenna temperature (taken to be 290 K), and the frequency-dependent empirical term is a parameterization for sky temperature based on [78]

$$P_N = K\beta \left\{ \left[44.6 \left(\frac{408 \times 10^6}{f} \right)^{2.47} \right] + T_{\text{ant}} \right\}.$$
 (10)

We consider four scenarios: pulse compressed data with an isotropic antenna pattern, unfocused data with an isotropic antenna pattern, SAR focused data with an isotropic antenna pattern, and SAR focused data with a cross-track array. For the purpose of this analysis, we consider a feature to be detectable so long as both the SCR and SNR exceed 0 dB.

Fig. 17 shows the detectability of various englacial features in pulse compressed data. The 45-MHz system has significantly better SCR, with smooth beds shallower than 2000 m already unaffected by clutter, whereas we expect clutter to dominate all 435-MHz data. The SNR, however, is the dominant constraint at this processing level, with all signals well below the noise floor. For example, the 45-MHz system would require approximately 30 dB of additional gain to detect those signals which are above the clutter floor—equivalent to increasing transmit power to 1 kW, pulselength to 850 μs , and antenna gain to 10 dB, for example. It is clear that azimuth processing will be critical to system performance regardless of frequency.

In the next scenario, we implement unfocused SAR processing by coherently summing traces over the diameter of the first Fresnel zone. This has the effect of both raising SNR by stacking and lowering clutter power by narrowing the effective beamwidth. Therefore, the results are highly sensitive to the choice of pulse repetition frequency (PRF). Fig. 18 shows the result of this analysis for a PRF of 242 Hz, the maximum

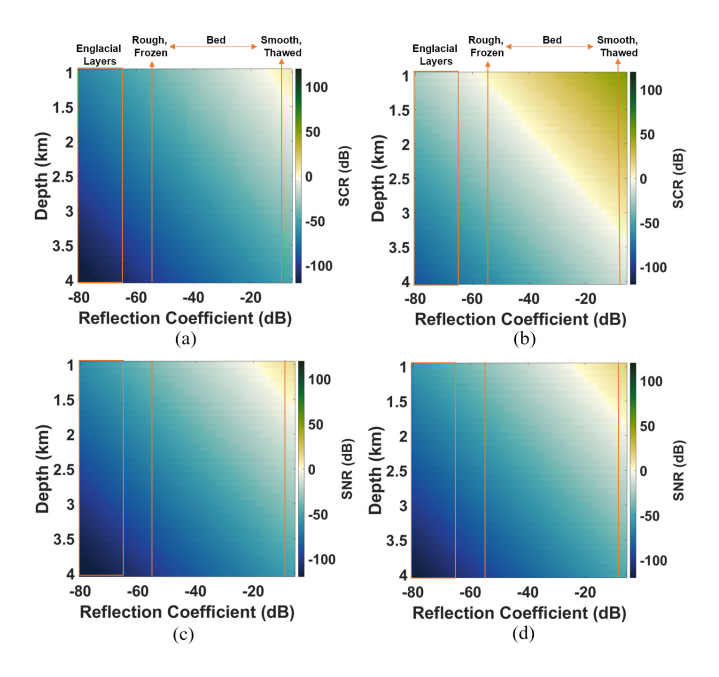


Fig. 17. Modeled SNR and SCR for an orbital sounder at 600 km altitude after pulse compression. An isotropic antenna beam pattern is assumed. (a) SCR at 435 MHz. (b) SCR at 45 MHz. (c) SNR at 435 MHz. (d) SNR at 45 MHz.

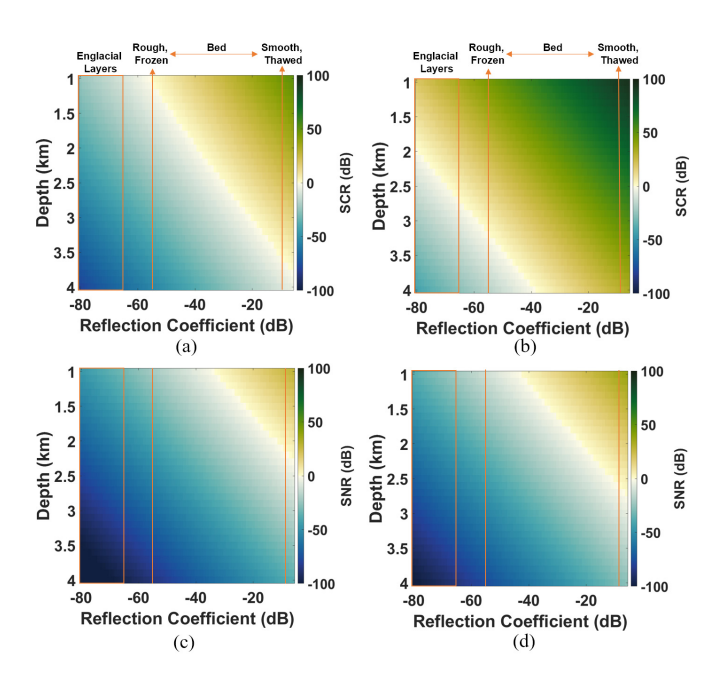


Fig. 18. Modeled SNR and SCR for an orbital sounder at 600 km altitude after coherent summation over the first Fresnel zone. An isotropic antenna beam pattern and PRF of 242 Hz is assumed. (a) SCR at 435 MHz. (b) SCR at 45 MHz. (c) SNR at 435 MHz. (d) SNR at 45 MHz.

PRF possible if we restrict the system to a single pulse in the air at a time. At 45 MHz, this is sufficient to overcome clutter for nearly all bed conditions shallower than 3000 m. While the 435-MHz SCR sees significant improvement, it is still insufficient to ensure the detection of more than shallow, thawed beds. Unfortunately, regardless of frequency, the SNR continues to lag. Even with a 100% duty cycle (equivalent to a PRF of 11.7 kHz at the assumed pulselength), coherent

-20

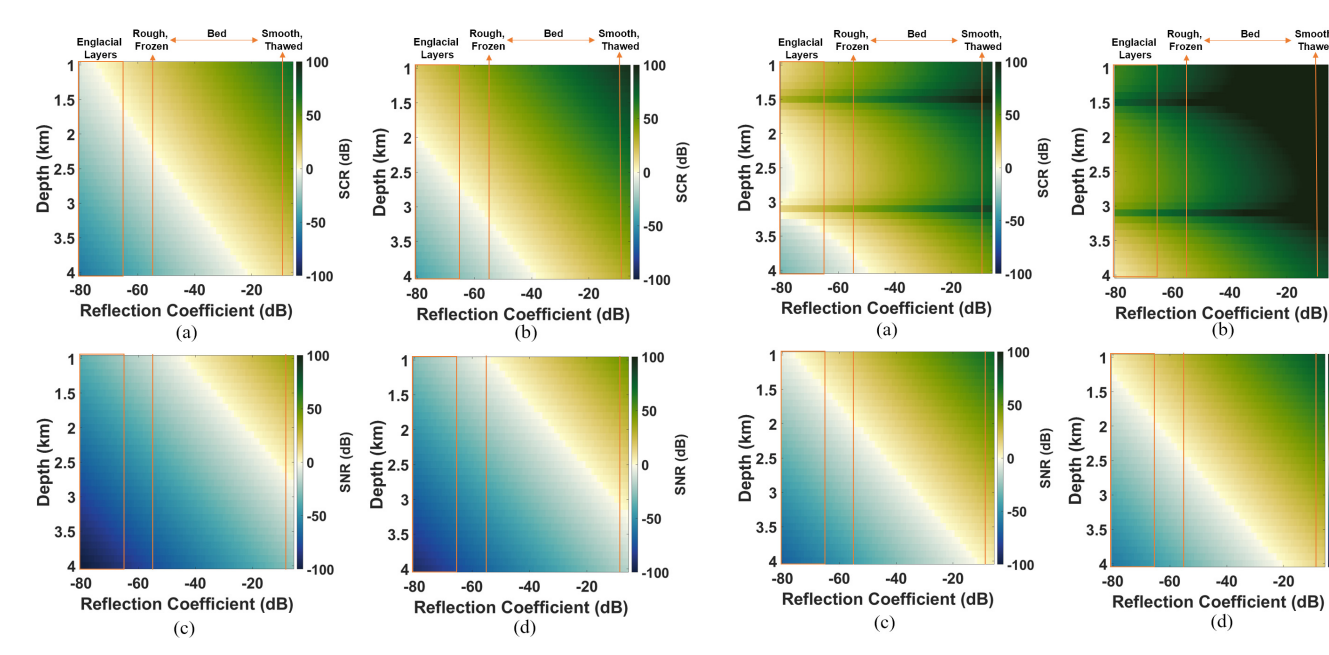


Fig. 19. Modeled SNR and SCR for an orbital sounder at 600 km altitude after SAR focusing using an aperture equal to ten times the diameter of the first Fresnel zone. An isotropic antenna beam pattern is assumed. (a) SCR at 435 MHz. (b) SCR at 45 MHz. (c) SNR at 435 MHz. (d) SNR at 45 MHz.

Fig. 20. Modeled SNR and SCR for an orbital sounder at 600 km altitude after SAR focusing using an aperture equal to ten times the diameter of the first Fresnel zone. A cross-track beamwidth of 2.5° is assumed. (a) SCR at 435 MHz. (b) SCR at 45 MHz. (c) SNR at 435 MHz. (d) SNR at 45 MHz.

summation over the Fresnel zone is insufficient to raise englacial layers or rough and frozen beds deeper than about 1500 m above the noise floor.

Focused SAR processing allows us to migrate power over a much longer distance than the first Fresnel zone while simultaneously improving the azimuth resolution of the data. Here, we consider an aperture length of ten times the diameter of the first Fresnel zone, with results shown in Fig. 19. This level of processing is sufficient to achieve reasonable SCR for both systems. For the 45-MHz system, we expect that clutter would only limit the detection of englacial layers deeper than 3000 m. At 435 MHz, englacial layers are still fully obscured by clutter, but we can detect all thawed beds and most frozen or rough beds shallower than 3000 m. Once again, SNR is the constraining factor in feature detection.

Finally, we consider the impact of implementing some forms of cross-track antenna array, in addition to SAR focusing. Here, we consider a half-power beamwidth of approximately 2.5°, equivalent to a linear array of 40 dipole elements at half-wavelength spacing. As shown in Fig. 20, this is sufficient to bring nearly all englacial signals above the level of the clutter at 435 MHz. However, this would require at least a 28 m cross-track array, which would be a significant technical challenge, far beyond existing heritage and high technical readiness level systems. However, this suggests that proposals for distributed sounding systems [79], [80] or other novel methods of cross-track array synthesis could significantly improve orbital system performance in the upper VHF or UHF bands. In addition, for airborne radar sounders, it is not unreasonable to consider using UHF center frequencies, given that cross-track half-power beamwidths on the order of 15° can achieve similar clutter suppression in airborne geometries, as demonstrated by the success of the CReSIS Ultra-Wideband sounder centered at 320 MHz [18].

Altogether, our analysis suggests that while HF and low VHF systems offer a significant advantage in near-surface clutter suppression, SNR will be the first constraining factor in bed detection for any orbital radar sounder. As a result, any system design must consider how to maximize the PRF for example, by using a burst mode [81]—and expect to implement full 2-D synthetic aperture focusing as a standard component of the data postprocessing routine. Given this baseline, a 435-MHz system is potentially viable, particularly as the shorter wavelength improves the feasibility of engineering a cross-track array. As the near-surface clutter gradient is relatively flat across the UHF band, it may even be feasible to consider L-band orbital sounding in the interior [82]. In this case, any frequency dependence of englacial attenuation and the scattering properties of the bed may place stronger constraints on the choice of center frequency than near-surface clutter. Alternately, suborbital platforms operating below the ionosphere might offer the possibility to operate in the HF band for clutter suppression while taking advantage of much slower flight velocities to improve SNR through increased integration time.

It may also be appropriate to adjust the choice of geophysical target to maximize the system performance. As expected, our analysis indicates that orbital sounding is most likely to be successful in regions with high basal reflection coefficients and low total attenuation. This suggests that particularly in Antarctica, sounding toward the ice sheet margins, where lower ice thickness, a shallower firn pack, and the presence of thawed beds [83]-[85] are more advantageous to the link budget, may not be significantly more difficult than sounding in the deep interior. The greatest challenges in these regions are surface and basal roughness and volume scattering, which require complementary optimization of azimuth processing methods and cross-track clutter suppression. We do not treat

heavy crevassing or temperate ice in fast-flowing regions, and these are likely to remain significant challenges for any radar system.

The implications of our analysis for orbital radar sounding of icy satellites and planets depend heavily on local environmental factors. The stratigraphy evident in the Martian polar ice caps, for example, is understood to be the result of the accumulation of water ice and dust layers shaped by climatic processes [15], [86], [87], strongly analogous to conditions in the terrestrial ice sheets. Our analysis, consistent with the success of the MARSIS and SHARAD missions, suggests that for such an environment, HF radar sounders are a safe choice. This is particularly true if there is evidence of ongoing accumulation since these rough layers are the intermediate product of compaction processes. Unfortunately, ionospheric attenuation and distortion make this an impractical choice for Earth-observing satellites [20]. On the other hand, in the absence of significant atmosphere, the metamorphic character of Europa's icy shell is likely shaped by internal marine, convective, or tectonic processes rather than accumulation [16], [88], [89], with the possible exception of potential plume deposits [90], [91]. Therefore, this type of near-surface clutter is unlikely to constrain the radar sounding of such environments. Together with recent optimistic assessments of volume scattering losses in icy regolith [92], this suggests that the VHF sounding of Europa may be limited by attenuation rather than clutter [89].

VIII. CONCLUSION

We find that for radar sounding in the VHF and UHF bands, dry polar firn behaves primarily as a stratigraphic, rather than volume scattering, medium, where scattering is dominated by quasi-specular reflection at interfaces between layers of different densities. Our results indicate that off-nadir scattering is likely controlled by scattering from small-scale roughness in the horizontal density profile that results from spatial variability in deposition and compaction patterns. As a result, the near surface may contribute significant clutter in stratigraphic environments with active accumulation. This clutter is weakest in the HF band, increases rapidly across the VHF band, and is effectively constant across the UHF spectrum. This suggests that for Earth-observing satellites, the low VHF range is ideal for near-surface clutter suppression. Increasing system bandwidth will generally improve performance under these clutter conditions, although the high fractional bandwidths required to achieve noticeable improvements are often impractical due to ITU spectrum allocations. Given these constraints, at 6-MHz bandwidth, a 45-MHz sounder offers on the order of 40 dB better firn clutter suppression than a 435-MHz sounder.

On terrestrial ice sheets, this type of quasi-specular layered firn is most common in the cold, high-elevation interior, where the mean ice thickness is on the order of 2600 m. Due to englacial attenuation in this thick ice, SNR, rather than SCR, will be the first constraining factor in bed detectability. Therefore, a critical consideration for system designers will be how to achieve high azimuth processing and antenna gain, regardless of the center frequency. Given these baseline requirements, UHF sounders may be viable, particularly if the

shorter wavelength permits implementation of a cross-track array which can improve both SCR and SNR. Alternately, designers might consider suborbital platforms or choose to optimize instruments for sounding toward the ice sheet margins where high basal reflectivities, thinner ice, and thinner firn are more advantageous to the system link budget.

APPENDIX A RADAR SOUNDING GEOMETRY MODEL

Here, we provide a detailed explanation of the sounding geometry model used to simulate the volume scattering and rough layer clutter power as a function of depth. The geometry under consideration is depicted in Fig. 1. We first consider the most basic geometry for unprocessed data collected with an isotropic antenna. In this case, the power received by the radar from a given depth, d, is the sum of the power backscattered from anywhere in the illuminated volume of the ice sheet where the round-trip time-of-flight falls within the following interval, where h is the platform altitude, $n_{\rm ice}$ is the index of refraction in ice, d is the target depth, δr_r is the system range resolution, and c is the speed of light in a vacuum:

$$\frac{2h}{c} + \frac{2n_{\text{ice}}\left(d - \delta r_r\right)}{c} < \tau \le \frac{2h}{c} + \frac{2dn_{\text{ice}}}{c}.\tag{11}$$

The received power at depth d is then the sum of the backscattered power over the entire volume defined by this interval. We assume that the englacial properties, such as porosity or layer roughness, which define the backscatter coefficient, change only with depth over the radar footprint. Therefore, we discretize the depth domain into layers of thickness Δz , calculate the backscattered power from each layer, and integrate over all layers to find the total received power.

The power backscattered by a layer is given by the standard radar equation [58]

$$P_R = \frac{P_T G^2 \lambda^2 T^2 L_{\text{ice}}^2}{(4\pi)^3 n_{\text{ice}}^2 \left(h + \frac{d}{n_{\text{ice}}}\right)^4} A \sigma^0.$$
 (12)

If we assume an isotropic antenna beam pattern, then the terms which change for each layer will be the illuminated area, A, the radar cross section of the layer, σ^0 , and the dielectric loss, $L^2_{\rm ice}$. A variety of models can be used to calculate σ^0 , depending on the relevant englacial properties. Similarly, $L^2_{\rm ice}$ can take a variety of forms. For now, we will assume the general form in (13), where d is the target depth and l is the generic one-way loss term which may be a function of the vertical position

$$L_{\text{ice}}^2 = \exp\left[-2ld\right]. \tag{13}$$

Therefore, we will describe how A is calculated, as this is general to the model. The models and assumptions used for σ^0 and L^2_{ice} will be discussed in the context of specific applications. In general, we assume that these coefficients are fixed over the illuminated area at a given depth.

At any given layer, A is a function of the platform altitude, target depth, system range resolution, and the index of refraction of ice. Specifically, it takes the form of an annulus, where the outer radius is fixed by the iso-delay curve of the

target range bin, and the inner radius is fixed by the isodelay curve of the next shallowest range bin (see Fig. 1). To calculate these radii at a given layer, we find the corresponding refraction point at the surface, following the methods discussed in [36] and [93], which allows us to then solve for the in-air and in-ice components of the geometric path. In our implementation, at each depth, we use a mean index of refraction through overlying firn layers, calculated from the B26 firn core density profile.

We implement various forms of radar focusing by adjustments to this raw scattering area. For unfocused SAR processing, the effective along-track beamwidth can be calculated from (14), where N is the number of coherent summations

$$\theta = \sin^{-1} \left[\frac{\left(\frac{\text{PRF}}{N}\right)\lambda}{2vn_f} \right]. \tag{14}$$

As shown in Fig. 1, sufficient coherent summations can restrict the along-track beamwidth to the extent that only cross-track portions of the illuminated annulus now contribute to the clutter. This restricted area can be derived from basic trigonometric relationships between beamwidth and platform viewing geometry, combined with the geometric formulas for a circular segment. Full synthetic aperture focusing can be dealt with similarly, where x, the along-track contributing extent, is set by the azimuth resolution of the focusing algorithm, which is given approximately by (15), where Λ is the length of the focusing aperture [24]

$$x = \frac{\lambda \left(h + \frac{d}{n_{\text{ice}}} \right)}{2\Lambda}.$$
 (15)

In addition, we can simulate the effect of a cross-track beam pattern by allowing G to vary over the illuminated area. We assume that the antenna pattern is isotropic along-track and uses an analytical approximation of the pattern of the form G(x, y) = f(y), where y is the cross-track direction and x is the along-track. G(x, y) is normalized to maximum power. Then, the antenna gain factor is the integral of the G(x, y) along the outer circumference of the illuminated area, normalized by the integral of an isotropic beam pattern over that same region.

Altogether, our geometry model takes the form given below, where the implementation of the various terms has been discussed above

$$P_{R}(z) = \frac{P_{T} \lambda^{2} T_{\text{ice}}^{2}}{(4\pi)^{3} n_{\text{ice}}^{2} \left(h + \frac{d}{n_{\text{ice}}}\right)^{4}} \times \left\{ \sum_{i=1}^{M} G_{i}^{2} \sigma_{i}^{0} A_{i} \Delta z_{i} * \exp\left[-2 \sum_{j=1}^{i} l_{j} \Delta z_{j}\right] \right\}$$
(16)

APPENDIX B

VOLUME SCATTERING RADAR EQUATION

Here, we discuss additions to the basic geometry model needed for the volume scattering calculations. The basic model is given in (16). From [44], if we assume that the target volume consists of independent scatterers, then the radar cross section of the scattering volume is equal to the total volume multiplied by the sum of the radar cross sections of

all particles in a unit volume

$$\sigma_v = V \sum_{i=1}^{N_v} \sigma_b. \tag{17}$$

V is the total illuminated volume, N_v is the number of scattering particles in a unit volume, and σ_b is the particle radar cross section. We will make two simplifying assumptions here. First, all particles in the scattering volume are spherical, and second, the variance in particle radius is very small compared to the illuminating wavelength. Under these conditions, we treat the volume as containing N identical particles of some mean radius r and dielectric constant ϵ . Then, (17) simplifies to

$$\sigma_v = V N_v \sigma_b (r, \epsilon) = N \sigma_b (r, \epsilon). \tag{18}$$

In order to calculate the total number of air-filled pores in the ice volume illuminated by the radar, we must account for the variable density of the firn. Within each discrete layer in the firn, the porosity is given by the following equation:

$$\phi_i = 1 - \frac{\rho_i}{\rho_{\text{ice}}}.\tag{19}$$

Here, ρ_i is the density of a given layer taken from the firn core profile and ρ_{ice} is the density of solid ice, taken to be 917 kg/m³. Then, the number of air pores in a given layer of firn is

$$N_i = V_i \phi_i \left(\frac{3}{4\pi r^3} \right) = A_i \Delta z_i \phi_i \left(\frac{3}{4\pi r^3} \right) \tag{20}$$

 V_i is the illuminated volume of the layer, which we already know to be $A_i \Delta z_i$ in our basic geometry model. Then, the total number of particles in the illuminated volume is simply the sum of the particles in each layer

$$N = \sum_{i=1}^{M} A_i \Delta z_i \phi_i \left(\frac{3}{4\pi r^3}\right). \tag{21}$$

Following [94], we take the two-way path loss through a layer to be $\exp[-2\tau]$, where τ is given by:

$$\tau = \frac{3\phi d}{4\pi r} \left[\xi_a \left(r, \epsilon \right) + \xi_s \left(r, \epsilon \right) \right]. \tag{22}$$

 ξ_a is the pore absorption efficiency and ξ_s is the pore scattering efficiency. The distance d traveled through the ice will be different for pores at different depths. Therefore, this attenuation factor will be different for each layer. We must also account for the variable porosity in the attenuating layers above the layer of interest. While, strictly speaking, the radar path length through each layer in the firn is a function of the platform viewing geometry, target depth, and layer index of refraction, we will make the simplifying assumption that this path length is roughly equal to the layer thickness. For an airborne platform sounding the shallow subsurface, this approximation will introduce around 1% error in the distance traveled through each layer, and less for an orbital platform

$$\tau = \sum_{j=1}^{i} \left(\frac{3}{4\pi r}\right) \phi_j \Delta z_j \left[\xi_a\left(r,\epsilon\right) + \xi_s\left(r,\epsilon\right)\right]. \tag{23}$$

Putting all of these components together, we derive the following approximate discretized volumetric radar equation for

$$R_{v} = \Gamma(\theta) + \left[\Gamma(0) - \Gamma(\theta)\right] \left(1 - \frac{S_{T}}{S_{T0}}\right)$$
(29)

$$S_T = \frac{|F_T|^2 \sum_{n=1}^{\infty} \frac{(k\sigma \cos\theta)^{2n}}{n!} W^n (2k\sin\theta)}{\sum_{n=1}^{\infty} \frac{(k\sigma \cos\theta)^{2n}}{n!} \left| F_T + \left(\frac{2^{n+2}\Gamma(0)}{\exp[(k\sigma \cos\theta)^2]\cos\theta} \right) \right|^2 W^n (2k\sin\theta)}$$
(30)

$$S_{T0} = \left| 1 + \frac{8\Gamma(0)}{F_T \cos \theta} \right|^{-2} \tag{31}$$

$$F_T = 8 |\Gamma(0)|^2 \sin^2 \theta \left(\frac{\cos \theta + \sqrt{\epsilon_r - \sin^2 \theta}}{\cos \theta \sqrt{\epsilon_r - \sin^2 \theta}} \right)$$
 (32)

monostatic radar sounding of the shallow subsurface:

$$P_{R}(z) = \frac{P_{T}G^{2}T^{2}\lambda^{2}}{(4\pi)^{3}n_{ice}^{2}\left(h + \frac{z}{n_{ice}}\right)^{4}}\sigma_{b}(r,\epsilon)$$

$$\times \left\{\sum_{i=1}^{M}A_{i}\Delta z_{i}\phi_{i}\left(\frac{3}{4\pi r^{3}}\right)\right.$$

$$\times \exp\left[-2\sum_{j=1}^{i}\Delta z_{j}\phi_{j}\left(\frac{3}{4\pi r}\right)\left[\xi_{a}(r,\epsilon) + \xi_{s}(r,\epsilon)\right]\right]\right\}.$$
(24)

APPENDIX C SIMPLIFIED INTEGRAL EQUATION METHOD

Here, we provide the full form of the vertically co-polarized coefficients used in the S-IEM scattering model. Full explanations of these terms can be found in [66]

$$I_{vv}^{n} = (2k\sigma\cos\theta)^{n} f_{vv} \exp[-(k\sigma\cos\theta)^{2}] + (k\sigma\cos\theta)^{n} F_{vv}$$

$$f_{vv} = \frac{2R_{v}}{\cos\theta}.$$
(26)

In the following terms, ϵ_r is the relative permittivity of the scattering interface. The S-IEM coefficients were derived assuming that the incident wave was in the air, with a permittivity of 1. However, we are interested in scattering when the wave is incident from a different layer of firn. Therefore, we use an effective ϵ_r which is chosen such that the difference in permittivity to air is equal to the difference in permittivity between the two firn layers of interest. This is a reasonable substitution since the reflection coefficients depend on the gradient of permittivity, rather than the absolute value. $\Gamma(\theta)$ is the p-polarized Fresnel reflection coefficient evaluated at the incidence angle of interest

$$F_{vv} = \left(\frac{\sin^2 \theta}{\cos \theta} - \frac{q}{\epsilon_r}\right) (1 + R_v)^2$$

$$-2\sin^2 \theta \left(\frac{1}{\cos \theta} + \frac{1}{q}\right) (1 + R_v) (1 - R_v)$$

$$+ \left[\frac{\sin^2 \theta}{\cos \theta} + \frac{\epsilon_r \left(1 + \sin^2 \theta\right)}{q}\right] (1 - R_v)^2$$

$$q = \sqrt{\mu_r \epsilon_r - \sin^2 \theta}.$$
(28)

The S-IEM model employs transition coefficients in place of the traditional Fresnel reflection coefficients, the forms of which are given in (29)–(32), as shown at the top of this page.

ACKNOWLEDGMENT

We acknowledge the use of data from CReSIS, as well as the CReSIS toolbox, generated with support from the University of Kansas, NASA Operation IceBridge Grant NNX16AH54G, NSF Grant ACI-1443054, Lilly Endowment Incorporated, and Indiana METACyt Initiative. Digital elevation models (DEMs) were provided by the Polar Geospatial Center under NSF-OPP awards 1043681, 1559691, and 1542736. We thank two anonymous reviewers for their thorough and constructive comments.

REFERENCES

- J. A. Dowdeswell and S. Evans, "Investigations of the form and flow of ice sheets and glaciers using radio-echo sounding," *Rep. Progr. Phys.*, vol. 67, no. 10, pp. 1821–1861, Aug. 2004.
- [2] S. Gogineni et al., "Coherent radar ice thickness measurement over the Greenland ice sheet," J. Geophys. Res., vol. 106, no. 24, pp. 33, 761–33, 772, 2001.
- [3] P. Fretwell et al., "Bedmap2: Improved ice bed, surface and thickness datasets for antarctica," Cryosphere Discuss., vol. 6, no. 5, pp. 4305–4361, 2013.
- [4] D. M. Schroeder, D. D. Blankenship, and D. A. Young, "Evidence for a water system transition beneath thwaites glacier, west antarctica," *Proc. Nat. Acad. Sci. USA*, vol. 110, no. 30, pp. 12225–12228, Jul. 2013.
- [5] W. Chu, D. M. Schroeder, and M. R. Siegfried, "Retrieval of englacial firn aquifer thickness from ice-penetrating radar sounding in southeastern greenland," *Geophys. Res. Lett.*, vol. 45, no. 21, pp. 11, 770–11, 778, Nov. 2018
- [6] T. M. Jordan et al., "A constraint upon the basal water distribution and thermal state of the Greenland Ice Sheet from radar bed echoes," Cryosphere, vol. 12, pp. 2831–2854, 2018.
- [7] R. G. Bingham and M. J. Siegert, "Radio-echo sounding over polar ice masses," J. Environ. Eng. Geophys., vol. 12, no. 1, pp. 47–62, Apr. 2007.
- [8] H. D. Pritchard, "Bedgap: Where next for antarctic subglacial mapping?" Antarctic Sci., vol. 26, no. 6, pp. 742–757, Nov. 2014.
- [9] E. Rignot et al., "Recent antarctic ice mass loss from radar interferometry and regional climate modelling," *Nature Geosci.*, vol. 1, no. 2, pp. 106–110, Jan. 2008.
- [10] D. M. Schroeder, A. M. Hilger, J. D. Paden, D. A. Young, and H. F. J. Corr, "Ocean access beneath the southwest tributary of pine island glacier, west antarctica," *Ann. Glaciol.*, vol. 59, no. 76, pp. 10–15, Dec. 2017.
- [11] J. J. Plaut et al., "Subsurface radar sounding of the south polar layered deposits of Mars," Science, vol. 316, no. 5821, pp. 92–95, Apr. 2007.
- [12] R. Seu et al., "SHARAD sounding radar on the Mars reconnaissance orbiter," J. Geophys. Res., Planets, vol. 112, no. E5, pp. 1–18, May 2007.
- [13] F. Rodriguez-Morales et al., "Development of a multi-frequency airborne radar instrumentation package for ice sheet mapping and imaging," in IEEE MTT-S Int. Microw. Symp. Dig., May 2010, pp. 157–160.

- [14] J. L. Whitten, B. A. Campbell, and G. A. Morgan, "Evaluating the structure of the south polar layered deposits on Mars using SHARAD data," in *Proc.* 47th Lunar Planet. Sci. Conf., 2016, pp. 5–6.
- [15] I. B. Smith, N. E. Putzig, J. W. Holt, and R. J. Phillips, "An ice age recorded in the polar deposits of Mars," *Science*, vol. 352, no. 6289, pp. 1075–1078, May 2016.
- [16] D. D. Blankenship, D. A. Young, W. B. Moore, and J. C. Moore, "Radar sounding of Europa's subsurface properties and processes: The view from Earth," in *Proc. Europa*, vol. 80, R. T. Pappalardo, W. B. McKinnon, and K. K. Khurana, Eds. Tucson, AZ, USA: Univ. of Arizona Press, 2017, pp. 631–654.
- [17] L. Bruzzone, G. Alberti, C. Catallo, A. Ferro, W. Kofman, and R. Orosei, "Subsurface radar sounding of the Jovian moon ganymede," *Proc. IEEE*, vol. 99, no. 5, pp. 837–857, May 2011.
- [18] Z. Wang et al., "Multichannel wideband synthetic aperture radar for ice sheet remote sensing: Development and the first deployment in antarctica," *IEEE J. Sel. Topics Appl. Earth Observ. Remote Sens.*, vol. 9, no. 3, pp. 980–993, Mar. 2016.
- [19] J. Dall et al., "ESA'S POLarimetric airborne radar ice sounder (POLARIS): Design and first results," *IET Radar, Sonar Navigat.*, vol. 4, no. 3, p. 488, 2010.
- [20] A. Freeman, X. Pi, and E. Heggy, "Radar sounding through the Earth's ionosphere at 45 MHz," *IEEE Trans. Geosci. Remote Sens.*, vol. 55, no. 10, pp. 5833–5842, Oct. 2017.
- [21] K. C. Jezek et al., "Two-frequency radar experiments for sounding glacier ice and mapping the topography of the glacier bed," *IEEE Trans. Geosci. Remote Sens.*, vol. 49, no. 3, pp. 920–929, Mar. 2011.
- [22] J. Li et al., "High-altitude radar measurements of ice thickness over the Antarctic and Greenland ice sheets as a part of operation icebridge," *IEEE Trans. Geosci. Remote Sens.*, vol. 51, no. 2, pp. 742–754, Feb. 2013.
- [23] D. Bekaert et al., "Multichannel surface clutter suppression: East Antarctica P-band SAR ice sounding in the presence of grating lobes," Ann. Glaciol., vol. 55, no. 67, pp. 9–21, Jul. 2017.
- [24] M. E. Peters, D. D. Blankenship, S. P. Carter, S. D. Kempf, D. A. Young, and J. W. Holt, "Along-track focusing of airborne radar sounding data from West Antarctica for improving basal reflection analysis and layer detection," *IEEE Trans. Geosci. Remote Sens.*, vol. 45, no. 9, pp. 2725–2736, Sep. 2007.
- [25] F. T. Ulaby, R. K. Moore, and A. K. Fung, Microwave Remote Sensing: Active and Passive, vol. 2. Reading, MA, USA: Addison-Wesley, 1982.
- [26] S. K. Nayar, K. Ikeuchi, and T. Kanade, "Surface reflection: Physical and geometrical perspectives," *IEEE Trans. Pattern Anal. Mach. Intell.*, vol. 13, no. 7, pp. 611–634, Jul. 1991.
- [27] G. Picardi et al., "Performance and surface scattering models for the Mars advanced radar for subsurface and ionosphere sounding (MarsIS)," Planet. Space Sci., vol. 52, nos. 1–3, pp. 149–156, Jan. 2004.
- [28] J. W. Holt, M. E. Peters, S. D. Kempf, D. L. Morse, and D. D. Blankenship, "Echo source discrimination in single-pass airborne radar sounding data from the Dry Valleys, Antarctica: Implications for orbital sounding of Mars," *J. Geophys. Res.*, vol. 111, no. E6, pp. 1–13, 2006.
- [29] J. Dall, "A backscattering and propagation model for radar sounding of ice sheets," in *Proc. IEEE Int. Geosci. Remote Sens. Symp. (IGARSS)*, Jul. 2016, pp. 7088–7091.
- [30] J. Dall, H. F. J. Corr, N. Walker, B. Rommen, and C.-C. Lin, "Sounding the Antarctic ice sheet from space: A feasibility study based on airborne P-band radar data," in *Proc. IEEE Int. Geosci. Remote Sens. Symp.* (IGARSS), Jul. 2018, pp. 4142–4145.
- [31] H. Miller and M. Schwager, "Density of ice core ngt37C95.2 from the North Greenland Traverse, dataset," PANGAEA Data Arch., 2000, doi: 10.1594/PANGAEA.57798.
- [32] Accumulation Radar Data, CReSIS, Lawrence, KS, USA, 2019.
- [33] Multi-channel Coherent Radar Depth Sounder Data, CReSIS, Lawrence, KS, USA, 2019.
- [34] CReSIS Toolbox, CReSIS, Lawrence, KS, USA, 2019.
- [35] J. A. MacGregor, D. P. Winebrenner, H. Conway, K. Matsuoka, P. A. Mayewski, and G. D. Clow, "Modeling englacial radar attenuation at Siple Dome, West Antarctica, using ice chemistry and temperature data," J. Geophys. Res., vol. 112, no. F3, pp. 1–14, Jul. 2007.
- [36] A. Heister and R. Scheiber, "Coherent large beamwidth processing of radio-echo sounding data," *Cryosphere Discuss.*, vol. 12, no. 9, pp. 2969–2979, 2018.

- [37] F. Rodriguez-Morales et al., "Advanced multifrequency radar instrumentation for polar research," *IEEE Trans. Geosci. Remote Sens.*, vol. 52, no. 5, pp. 2824–2842, May 2014.
- [38] J. D. Paden. Radar Depth Sounder README. CReSIS Data Products. Accessed: Oct. 23, 2019. [Online]. Available: ftp://data.cresis.ku.edu/data/rds/rds_readme.pdf
- [39] J. D. Paden. Accumulation Radar README. CReSIS Data Products. Accessed: Oct. 23, 2019. [Online]. Available: ftp://data.cresis.ku.edu/data/accum/accum_readme.pdf
- [40] J.-B. Yan et al., "Measurements of in-flight cross-track antenna patterns of radar depth Sounder/Imager," *IEEE Trans. Antennas Propag.*, vol. 60, no. 12, pp. 5669–5678, Dec. 2012.
- [41] A. K. Kendrick *et al.*, "Surface meltwater impounded by seasonal englacial storage in west greenland," *Geophys. Res. Lett.*, vol. 45, no. 19, pp. 10, 474–10, 481, Oct. 2018.
- [42] F. Baumgartner, K. C. Jezek, R. R. Forster, S. Gogineni, and I. H. H. Zabel, "Spectral and angular ground-based radar backscatter measurements of greenland snow facies," in *Proc. IGARSS*, 1999, pp. 1053–1055.
- [43] B. S. Yurchak, "Some features of the volume component of radar backscatter from thick and dry snow cover," in *Advances in Geoscience* and *Remote Sensing*. London, U.K.: IntechOpen, 2009, pp. 1–140.
- [44] F. T. Ulaby and D. G. Long, Microwave Radar and Radiometric Remote Sensing. Ann Arbor, MI, USA: Univ. of Michigan Press, 2014.
- [45] A. Burr, C. Ballot, P. Lhuissier, P. Martinerie, C. L. Martin, and A. Philip, "Pore morphology of polar firn around closure revealed by Xray tomography," *Cryosphere*, vol. 12, no. 7, pp. 2481–2500, Jul. 2018.
- [46] R. B. Alley, J. F. Bolzan, and I. M. Whillans, "Polar firn densification and grain growth," *Ann. Glaciol.*, vol. 3, pp. 7–11, Jan. 2017.
- [47] R. Lomonaco, M. Albert, and I. Baker, "Microstructural evolution of fine-grained layers through the firn column at summit, greenland," *J. Glaciol.*, vol. 57, no. 204, pp. 755–762, 2011.
- [48] S. Fujita et al., "Nature of radio echo layering in the antarctic ice sheet detected by a two-frequency experiment," J. Geophys. Res., Solid Earth, vol. 104, no. B6, pp. 13013–13024, Jun. 1999.
- [49] C. Lewis et al., "Airborne fine-resolution UHF radar: An approach to the study of englacial reflections, firn compaction and ice attenuation rates," J. Glaciol., vol. 61, no. 225, pp. 89–100, Jul. 2017.
- [50] S. A. Arcone, V. B. Spikes, and G. S. Hamilton, "Phase structure of radar stratigraphic horizons within antarctic firn," *Ann. Glaciol.*, vol. 41, pp. 10–16, Sep. 2017.
- [51] B. Medley, S. R. M. Ligtenberg, I. Joughin, M. R. Van den Broeke, S. Gogineni, and S. Nowicki, "Antarctic firn compaction rates from repeat-track airborne radar data: I. Methods," *Ann. Glaciol.*, vol. 56, no. 70, pp. 155–166, Jul. 2017.
- [52] T. Laepple, M. Hörhold, T. Münch, J. Freitag, A. Wegner, and S. Kipfstuhl, "Layering of surface snow and firn at Kohnen Station, Antarctica: Noise or seasonal signal?" J. Geophys. Res., Earth Surf., vol. 121, no. 10, pp. 1849–1860, Oct. 2016.
- [53] M. Proksch, H. Löwe, and M. Schneebeli, "Density, specific surface area, and correlation length of snow measured by high-resolution penetrometry," *J. Geophys. Res., Earth Surf.*, vol. 120, no. 2, pp. 346–362, Feb. 2015.
- [54] K. Klein, "Variability in dry Antarctica firn: Investigations on spatially distributed snow and firn samples from Dronning Maud land, Antarctica," Ph.D. dissertation, Alfred Wegener Inst., Univ. Bremen, Bremen, Germany, 2018. Accessed: Mar. 3, 2020. [Online]. Available: https://epic.awi.de/id/eprint/37116/
- [55] J. A. MacGregor et al., "Radiostratigraphy and age structure of the greenland ice sheet," J. Geophys. Res., Earth Surf., vol. 120, no. 2, pp. 212–241, Feb. 2015.
- [56] M. Studinger, "IceBridge ATM L1B elevation and return strength, version 2," NASA Nat. Snow Ice Data Center Distrib. Act. Arch. Center, Boulder, CO, USA, Tech. Rep. 20140508_171546, 2013.
- [57] M. Studinger, "IceBridge ATM L1B Qfit elevation and return strength, version 1," NASA National Snow Ice Data Center Distrib. Act. Arch. Center, Boulder, CO, USA, Tech. Rep. 20110506_133429,134057, 2010.
- [58] M. E. Peters, "Analysis techniques for coherent airborne radar sounding: Application to west antarctic ice streams," *J. Geophys. Res.*, vol. 110, no. B6, pp. 1–17, 2005.
- [59] S. Linow, M. W. Hörhold, and J. Freitag, "Grain-size evolution of polar firn: A new empirical grain growth parameterization based on X-ray microcomputer tomography measurements," *J. Glaciol.*, vol. 58, no. 212, pp. 1245–1252, 2012.

- [60] A. Kovacs, A. J. Gow, and R. M. Morey, "A reassessment of the in-situ dielectric constant of polar firn," Cold Regions Res. Eng. Lab., Hanover, NH, USA, Tech. Rep. CRREL-93-26, Dec. 1993.
- [61] C. Grima, D. D. Blankenship, D. A. Young, and D. M. Schroeder, "Surface slope control on firn density at Thwaites Glacier, West Antarctica: Results from airborne radar sounding," *Geophys. Res. Lett.*, vol. 41, no. 19, pp. 6787–6794, Oct. 2014.
- [62] P. Yeh, Optical Waves in Layered Media. Hoboken, NJ, USA: Wiley, 2005.
- [63] R. M. Gray and L. D. Davisson, An Introduction to Statistical Signal Processing. Cambridge, MA, USA: Cambridge Univ. Press, 2004.
- [64] C. Grima, D. M. Schroeder, D. D. Blankenship, and D. A. Young, "Planetary landing-zone reconnaissance using ice-penetrating radar data: Concept validation in Antarctica," *Planet. Space Sci.*, vol. 103, pp. 191–204, Nov. 2014.
- [65] R. C. A. Hindmarsh, G. J.-M.-C. L. Vieli, M. J. Raymond, and G. H. Gudmundsson, "Draping or overriding: The effect of horizontal stress gradients on internal layer architecture in ice sheets," *J. Geophys. Res.*, vol. 111, no. F2, pp. 1–17, 2006.
- [66] A. K. Fung and K. S. Chen, "The simplified integral equation surface backscattering model," in *Microwave Scattering and Emission Mod*els and Their Applications. Boston, MA, USA: Artech House, 2010, pp. 47–52.
- [67] M. S. Haynes, E. Chapin, and D. M. Schroeder, "Geometric power fall-off in radar sounding," *IEEE Trans. Geosci. Remote Sens.*, vol. 56, no. 11, pp. 6571–6585, Nov. 2018.
- [68] D. LeVine, "The radar cross section of dielectric disks," *IEEE Trans. Antennas Propag.*, vol. AP-32, no. 1, pp. 6–12, Jan. 1984.
- [69] C. Porter et al., "ArcticDEM, V1, dataset," Harvard Dataverse, 2018, doi: 10.7910/DVN/OHHUKH.
- [70] C. Grima, W. Kofman, A. Herique, R. Orosei, and R. Seu, "Quantitative analysis of Mars surface radar reflectivity at 20 MHz," *Icarus*, vol. 220, no. 1, pp. 84–99, Jul. 2012.
- [71] H. Oerter et al., "Physical properties and accumulation rates in Dronning Maud Land, Antarctica, dataset," PANGAEA Data Arch., 2000, doi: 10.1594/PANGAEA.728162.
- [72] S. Gerland and F. Wilhelms, "Continuous density log of ice core BER11C95_25, dataset," PANGAEA Data Arch., 1999, doi: 10.1594/PANGAEA.227732.
- [73] F. Wilhelms, "Density of ice core ngt27c94.2 from the North Greenland Traverse, dataset," PANGAEA Data Arch., 2000, doi: 10.1594/PAN-GAEA.57296.
- [74] B. A. Campbell, D. M. Schroeder, and J. L. Whitten, "Mars radar clutter and surface roughness characteristics from MARSIS data," *Icarus*, vol. 299, pp. 22–30, Jan. 2018.
- [75] C. H. Harrison, "Radio echo sounding of horizontal layers in ice," J. Glaciol., vol. 12, no. 66, pp. 383–397, 1973.
- [76] K. Matsuoka, J. A. MacGregor, and F. Pattyn, "Predicting radar attenuation within the antarctic ice sheet," *Earth Planet. Sci. Lett.*, vols. 359–360, pp. 173–183, Dec. 2012.
- [77] S. Ramongassie, P. Valle, P. G. Arpesi, and F. Heliere, "P-band SAR instrument for biomass," in *Proc. Eur. Conf. Synth. Aperture Radar* (EUSAR), 2014, pp. 1156–1159.
- [78] J. Ralston, J. Heagy, and R. Sullivan, "Environmental/noise effects on VHF/UHF UWB SAR," Inst. Defense Analyses, Alexandria, VA, USA, Tech. Rep. P-3385, Sep. 1998.
- [79] P. Gogineni et al., "A CubeSat train for radar sounding and imaging of antarctic ice sheet," in Proc. IEEE Int. Geosci. Remote Sens. Symp. (IGARSS), Jul. 2018, pp. 4138–4141.
- [80] L. Carrer, C. Gerekos, and L. Bruzzone, "Distributed radar sounder system: A novel approach to across-track resolution enhancement and clutter reduction," in *Proc. IEEE Int. Geosci. Remote Sens. Symp.* (IGARSS), Jul. 2018, pp. 6765–6768.
- [81] R. K. Raney, "CryoSat SAR-mode looks revisited," *IEEE Geosci. Remote Sens. Lett.*, vol. 9, no. 3, pp. 393–397, May 2012.
- [82] J.-B. Yan, P. Gogineni, and C. O'Neill, "L-band radar sounder for measuing ice basal conditions and ice-shelf melt rate," in *Proc. IEEE Int. Geosci. Remote Sens. Symp. (IGARSS)*, Jul. 2018, pp. 4135–4137.
- [83] J. A. MacGregor et al., "A synthesis of the basal thermal state of the greenland ice sheet," J. Geophys. Res., Earth Surf., vol. 121, no. 7, pp. 1328–1350, Jul. 2016.
- [84] D. W. Ashmore and R. G. Bingham, "Antarctic subglacial hydrology: Current knowledge and future challenges," *Antarctic Sci.*, vol. 26, no. 6, pp. 758–773, Nov. 2014.

- [85] F. Pattyn, "Antarctic subglacial conditions inferred from a hybrid ice sheet/ice stream model," *Earth Planet. Sci. Lett.*, vol. 295, nos. 3–4, pp. 451–461. Jul. 2010.
- [86] R. J. Phillips et al., "Mars north polar deposits: Stratigraphy, age, and geodynamical response," Science, vol. 320, no. 5880, pp. 1182–1185, May 2008.
- [87] N. E. Putzig et al., "Subsurface structure of Planum Boreum from Mars Reconnaissance Orbiter shallow radar soundings," *Icarus*, vol. 204, no. 2, pp. 443–457, Dec. 2009.
- [88] B. E. Schmidt, D. D. Blankenship, G. W. Patterson, and P. M. Schenk, "Active formation of 'chaos terrain' over shallow subsurface water on Europa," *Nature*, vol. 479, no. 7374, pp. 502–505, Nov. 2011.
- [89] K. Kalousová, D. M. Schroeder, and K. M. Soderlund, "Radar attenuation in Europa's ice shell: Obstacles and opportunities for constraining the shell thickness and its thermal structure," *J. Geophys. Research: Planets*, vol. 122, no. 3, pp. 524–545, Mar. 2017.
- [90] L. Roth et al., "Transient water vapor at Europa's south pole," Science, vol. 343, no. 6167, pp. 171–174, 2014.
- [91] W. B. Sparks et al., "Active cryovolcanism on Europa?" Astrophys. J., vol. 839, no. 2, p. L18, Apr. 2017.
- [92] Y. Aglyamov, D. M. Schroeder, and S. D. Vance, "Bright prospects for radar detection of Europa's ocean," *Icarus*, vol. 281, pp. 334–337, Jan. 2017.
- [93] F. Heliere, C.-C. Lin, H. Corr, and D. Vaughan, "Radio echo sounding of Pine Island Glacier, West Antarctica: Aperture synthesis processing and analysis of feasibility from space," *IEEE Trans. Geosci. Remote Sens.*, vol. 45, no. 8, pp. 2573–2582, Aug. 2007.
- [94] J. Eluszkiewicz, "Dim prospects for radar detection of Europa's ocean," *Icarus*, vol. 170, no. 1, pp. 234–236, Jul. 2004.



Riley Culberg (Student Member, IEEE) received the B.S. degree in computer science and geospatial information science from the United States Military Academy, West Point, NY, USA, in 2012, and the M.S. degree in electrical engineering from Stanford University, Stanford, CA, USA, in 2019, where he is currently pursuing the Ph.D. degree in electrical engineering.

He is a Member of the Stanford Radio Glaciology Research Group, Department of Geophysics, Stanford University, where he is involved in investigating

the near-surface structure of the continental ice sheets and its control on glacial hydrology using airborne radar sounding and electromagnetic modeling.

Mr. Culberg received the U.S. Department of Defense National Defense Science and Engineering Graduate Fellowship.



Dustin M. Schroeder (Senior Member, IEEE) received the B.A. degree in physics and the B.S.E.E. degree (mangacum laude) in electrical engineering from Bucknell University, Lewisburg, PA, USA, in 2007, and the Ph.D. degree in geophysics from the University of Texas at Austin, Austin, TX, USA, in 2014.

He is currently an Assistant Professor of geophysics and (by courtesy) electrical engineering with Stanford University, Stanford, CA, USA, where he is also a Faculty Member with the Stanford Woods

Institute for the Environment. His research group seeks to approach problems from both an earth system science and a radar system engineering perspective. He participated in three Antarctic field seasons with the Investigating the Cryospheric Evolution of the Central Antarctic Plate (ICECAP) Project and NASA's Operation Ice Bridge as a Radar Engineer and an Operator. His research interests include observing and understanding the role that subglacial water plays in the evolution and stability of continental ice sheets and their contribution to the rate of sea-level rise, development, use, and analysis of geophysical radar remote sensing systems that are optimized to observe hypothesis-specific phenomena.

Dr. Schroeder is a Science Team Member on the REASON instrument on NASA's Europa Clipper Mission and the Mini-RF instrument on NASA's Lunar Reconnaissance Orbit.